Monthly Notices of the ROYAL ASTRONOMICAL SOCIETY

MNRAS **523,** 286–304 (2023) https://doi.org/10.1093/mnras/stad1251
Advance Access publication 2023 April 29

AIOLOS – A multipurpose 1D hydrodynamics code for planetary atmospheres

Matthäus Schulik [1]★ and Richard A. Booth [1,2]

[1]*Astropysics group, Department of Physics, Imperial College London, Prince Consort Road, London SW7 2AZ, UK*
[2]*School of Physics and Astronomy, University of Leeds, Leeds LS2 9JT, UK*

Accepted 2023 April 11. Received 2023 April 6; in original form 2022 July 13

ABSTRACT

We present a new 1D multiphysics simulation code with use cases intended for, but not limited to, hydrodynamic escape problems of planetary atmospheres and planetary accretion models. Our formulation treats an arbitrary number of species as separated hydrodynamic fields, couples them via friction laws, allows for a multiband flux-limited radiation transport, and tracks ionization fronts in high-energy irradiation bands. Besides coupling various known numerical solution techniques together, we improve on the numerical stability of deep hydrostatic atmospheres by using a well-balanced scheme, hence preventing unphysical driving of atmospheric in- or outflow. We demonstrate the correct physical behaviour of the individual code modules and present a few simple, new applications, such as a proof-of-concept simulations of combined core-powered mass-loss and UV-driven atmospheric escape, along with a fully time-dependent core-collapse giant planet simulation. The multispecies nature of the code opens up the area of exploring simulations that are agnostic towards the dominant atmospheric species and can lead to implementations of advanced planetary evolution schemes.

Key words: hydrodynamics – radiative transfer – planets and satellites: atmospheres – planets and satellites: gaseous planets .

1 INTRODUCTION

The exoplanet population as it presents itself to the scientific community today exhibits a number of striking features. Those features manifest themselves in the data as gaps in the period–radius and period–mass distributions that are upheld after bias corrections (Mayor et al. 2011; Fulton et al. 2017; Van Eylen et al. 2018; Ho & Van Eylen 2023). The period–radius gap at small planetary radii of $\sim 1.7 R_\oplus$ is often interpreted as a sign of past and efficient hydrodynamic escape (Owen & Wu 2017; Ginzburg, Schlichting & Sari 2018), an imprint of the formation semimajor-axis in the protoplanetary disc (Lee & Connors 2021; Lee, Karalis & Thorngren 2022) or of compositional differences of the planetary bulk (Zeng et al. 2019). Furthermore, the paucity in intermediate-radius planets at high planetary equilibrium temperatures (Mayor et al. 2011) is often interpreted as a relic of unsuccessful runaway gas-accretion (Mordasini et al. 2012) owing to an exceedingly long phase of quasi-hydrostatic gas-envelope growth around massive cores (Pollack et al. 1996) under high-opacity disc conditions (Movshovitz et al. 2010).

Both of these mechanisms, gas accretion (Mizuno, Nakazawa & Hayashi 1978; Bodenheimer & Pollack 1986; Wuchterl 1990; Piso & Youdin 2014) and hydrodynamic escape (Öpik 1963; Hunten 1973; Sekiya, Nakazawa & Hayashi 1980; Watson, Donahue & Walker 1981; Zahnle & Kasting 1986; Yelle 2004; Lammer et al. 2008), have a long history of being studied theoretically under various assumptions, going back to the works of Bondi (1952) and Parker (1958). While various modern codes exist to simulate those processes in dynamical multidimensional simulations (Kley 1998; D'Angelo, Kley & Henning 2003; Vidal-Madjar et al. 2004; Ayliffe & Bate 2009; Tanigawa, Ohtsuki & Machida 2012; McCann et al. 2019), these codes employ simplifications to the computed physics due to their enormous computational cost. We prioritize developing the multiphysics aspect of a 1D code in this work, as we ultimately aim for evolutionary simulations covering significant multiples of dynamical atmospheric time-scales. Furthermore we aim to follow the evolution of the planetary atmospheric composition through in- and outflows.

Particularly when considering that in the context of planet formation and evolution, accretion and escape processes act subsequently, it is desirable to write a simulation code which can compute both situations reliably, while simultaneously expanding upon past work.

From the standpoint of numerical simulations, such a code therefore should be able to capture transonic phenomena, handle optically thin-to-thick transitions and reproduce hydrostatic equilibria in a numerically stable manner. All those properties are required in a dynamical simulation, as the states of atmospheric accretion and escape can be understood as non-linear perturbations on top of an initially hydrostatic state, where only the sign of the pressure perturbation differs.

The sign of this perturbation depends on whether heating or cooling is more important in a given atmospheric region. While accretion will be driven by bolometric cooling and self-gravity (Hubeny 1990; Pollack et al. 1996), atmospheric escape can be powered both by bolometric (Ginzburg et al. 2018; Gupta & Schlichting 2019, 2020) and high-energy irradiation (Sekiya et al. 1980; Lammer et al. 2003; Yelle 2004; García Muñoz 2007; Murray-Clay, Chiang & Murray 2009; Owen & Jackson 2012; Erkaev et al. 2013; Salz et al. 2016; Kubyshkina et al. 2018, 2019; Caldiroli et al. 2021). Recent studies have particularly targeted the relative importance of the latter two

★ E-mail: mschulik@ic.ac.uk

processes for planetary evolution (Rogers & Owen 2020; Rogers et al. 2021), but *ab initio* simulations of bolometrically driven mass-loss (i.e. core-powered mass-loss) and a unified and physically consistent bolometric-UV simulation framework have not been conducted. While previous work did employ full irradiation spectra (e.g. Salz et al. 2015; Kubyshkina et al. 2018), those codes rely on prescribing conditions in the lower atmosphere via boundary conditions, and omit the outgoing radiation field. We aim to improve upon those previous works by following the photon energies deep into the diffusive parts of the atmosphere, in principle down to the planetary surface. This opens up new classes of radiation hydrodynamic outflow solutions, i.e. those with temperature inversions and those for which re-radiation is important (e.g. Booth, Owen & Schulik 2023)

In the numerical context, traditional codes lack some important aspects which are desired to solve a hydrodynamic multispecies problem with bolometric and high-energy radiation transport, hence we now briefly outline our technical reasoning for presenting a new simulation code.

First, and most importantly, modern Riemann solvers suffer from problems keeping a hydrostatic solution stable against gravity source terms, a problem already described in Greenberg & Leroux (1996). A naive approach in trying to balance a fluid will induce oscillations that result in catastrophic imbalances (Käppeli & Mishra 2016; hereafter KM16) because the cell-centred gravitational source does not 'know' about the pressure differences that were passed to the interface-centred Riemann fluxes, and therefore cannot exactly fulfill a hydrostatic balance condition against them. An alternative for this is to include the gravitational flux in the Riemann solver (Colella & Woodward 1984), which would require a new numerical flux function and an efficient and correct approximation to this numerical flux, which is generally not a trivial task to solve (Toro, Spruce & Speares 1994).

To get around those problems, one can aim to *well-balance* sources and flux differences in the cell in order to generate zero net momentum evolution in cases when the cell boundary fluxes obey certain conditions. A possible approach, which we employ throughout this work, is given in e.g. Käppeli & Mishra (2014) and KM16, where a reconstruction approach is used to correct the pressure at cell interfaces with information about the force balance which needs to be fulfilled. This allows a time-dependent simulation to remain stable against oscillations as well as increasing the fidelity of hydrodynamic states in the deep, near-hydrostatic atmosphere.

Furthermore, in moving fluid regions, the tracking of velocities and temperatures of individual particle species is important (Schunk 1977) in order to determine whether they escape or remain hydrostatic (Zahnle & Kasting 1986). As particles interact with each other collisionally, it is required to solve for the rates of their momentum and internal energy exchange as well. Only then accurate velocities and escape/accretion rates for all species can be obtained.

Single-fluid formulations often avoid solving this problem by evolving an individual species density in a diffusion approximation, while a single velocity average and temperature variable exists for all species. Those formulations can be problematic and unflexible, however, and can lead to inaccurate low-density behaviour already in two-species solutions (Zahnle & Kasting 1986). The process of collisional decoupling is important in upper planetary atmospheres (Schunk & Nagy 1980), where each (partially ionized) plasma species can develop their own temperatures and velocities. In reality, this process is often aided by magnetic fields (Lammer et al. 2008; Gunell et al. 2018), which we entirely neglect in our work, but monemtum or thermal decoupling can still play a major role for the atmospheric evolution. We use a recently presented method by Benítez-Llambay, Krapp & Pessah (2019) for linearized drag-laws that allows the frictional coupling of an arbitrary number of species. We employ their formulation and develop a consistent formulation for the heat exchange terms into our temperature solver, which allows us to correctly represent any coupling strength.

Effects of radiation transport on atmospheric outflows are often treated in the popular energy-limited escape approximation (Watson et al. 1981; Lammer et al. 2003; Baraffe et al. 2004; Owen 2019). This formulation neglects radiative losses completely, or re-introduces them as non-thermal cooling functions Murray-Clay et al. (2009), Johnstone et al. (2018), and Kubyshkina et al. (2018, 2019) without ray-tracing. The escape rate is then given by balancing the cooling-corrected stellar high-energy heating with the adiabatic expansion of the atmosphere into space. Selecting the high-energy parts of the stellar radiation spectrum for an energy-limited escape treatment while neglecting the thermal photon field is justified by the inefficient thermalization of atomic species with the ambient thermal photon field (Sekiya et al. 1980; Erkaev et al. 2007; Owen & Alvarez 2016; Salz et al. 2016; Kubyshkina et al. 2018). Molecular species on the other hand have dense line forests, making them efficient at losing energy towards the ambient thermal photon field. Those species can then develop complex thermal profiles (Guillot 2010; Parmentier & Guillot 2014; Parmentier et al. 2015). The effects of those thermal profiles on atmospheric escape have not yet been characterized, which is required in order to properly characterize core-powered mass-loss. It is therefore desirable to obtain a code that can erase the artificial dividing line between the heating/cooling physics of molecules, atoms, the singling out of hand-selected parts of the instellation spectrum, as well as solve for the transition between them via photodissociation and recombination.

To this end, we present AIOLOS, a new public.[1], time-dependent 1D multispecies, multiband, radiation-hydrodynamics code. In Section 2, we first present the physical equations solved. In Section 3, we present and discuss the numerical schemes used for hydrostatic well-balancing, drag, radiation transport, and photochemistry. Section 4–7 shows the performance of those individual physics modules compared against analytical solutions or numerical solutions from the literature. Section 8 presents two new applications that our approach enables. In Section 9, we finally discuss limitations in our approach and an outlook.

2 EQUATIONS SOLVED

AIOLOS solves the equations of multispecies radiation-hydrodynamics in one dimension, in either cartesian, cylindrical, or spherical coordinates. All results discussed in this paper are computed in spherical coordinates, as is usual for planetary applications, except for shock tube tests, which are performed in cartesian geometry. Each species is treated by solving an independent set of Euler equations. Note that we list the most important variables in Table 1 for clarity. The different species coupled together via collisions, radiative heating and cooling, and photochemistry. Explicitly, for each species, s, the density, ρ_s, momentum, $\rho_s u_s$, and total energy, $E_s = \frac{1}{2}\rho_s u_s^2 + \rho_s e_s$, obey

$$\frac{\partial \rho_s}{\partial t} + \nabla \cdot [\rho_s u_s] = Q_s, \tag{1}$$

$$\frac{\partial \rho_s u_s}{\partial t} + \nabla \cdot [\rho_s u_s^2 + p_s] = -\rho_s \nabla \Phi + \frac{\mathrm{d}\mathcal{M}_s}{\mathrm{d}t} + Q'_s, \tag{2}$$

[1]See https://github.com/Schulik/aiolos

Table 1. Definitions of important quantities and those at risk of being confused. Most quantities are functions of r, unless otherwise stated. Other variables relevant to specific modules, e.g. collision frequencies, flux-limited diffusion parameters etc. have low confusion probability and are introduced on the spot.

Symbol	Description
i or j	Cell-centered index
$i + 1/2$ or $j + 1/2$	Cell interface index
$r_{i+1/2}$	Radius at cell interface $i + 1/2$
m_s	Particle mass in species s in (g)
ρ_s	Conserved volumetric mass density in species s in (g cm^{-3})
E_s	Conserved volumetric total energy density in species s in (erg cm^{-3})
e_s	Primitive specific internal energy density in species s in (erg g^{-1})
n_s	Primitive volumetric number density in species s in (cm^{-3})
u_s	Primitive velocity in species s in (cm s^{-1})
p_s	Primitive pressure in species s in (erg cm^{-3})
T_s	Kinetic temperature in species s in (K)
J^b	Mean photon intensity in band b in (erg cm^{-2} s^{-1})
$T^b_{\rm rad}$	Radiation temperature in band b in (K)
F^b	Outgoing photon flux in band b in (erg cm^{-2} s^{-1})
H	Harvard radiative flux $F/4\pi$
$f^b(T_b)$	Fraction of blackbody integral at temperature T^b in band b in (1)
$S^b(r)$	Stellar irradiation flux in band b, a function of r in (erg cm^{-2} s^{-1})
$S^{\odot,\,b}$ or $S^{\odot}_b$	Top-of-atmosphere stellar irradiation flux in band b, a constant in (erg cm^{-2} s^{-1})
$\Delta S_s(r)$	Stellar heating function per species, i.e. a sum over the absorbed fluxes in all bands, in (erg cm^{-3} s^{-1})
$\kappa^b_{\odot}$, $\tau^b_{\odot}$	Opacity and optical depth to stellar irradiation $S^b(r)$, functions of r
$\boldsymbol{F}_s$	Hydrodynamic flux for species s in g $\times$ $\left(\text{cm}^{-2}\text{s}^{-1},\ \text{cm}^{-1}\text{s}^{-2},\ \text{s}^{-3}\right)$
Φ	Gravitational potential in (erg g^{-1})

$$\frac{\partial E_s}{\partial t} + \nabla \cdot [u_s(E_s + p_s)] = -u_s \rho_s \nabla \Phi + u_s \frac{\mathrm{d}\mathcal{M}_s}{\mathrm{d}t} + \frac{\mathrm{d}\mathcal{E}_s}{\mathrm{d}t} + \Gamma_s. \quad (3)$$

Here, p_s is the partial pressure of the species, e_s is the internal energy per unit volume, and Φ is the gravitational potential. We close these equations with the adiabatic equation of state $p_s = (\gamma_s - 1)\rho_s e_s$ and ideal gas equations of state for the specific internal energy, i.e. $e_s = c_{v,\,s} T_s$. The adiabatic index γ_s is computed from the species degrees of freedom f_s via $\gamma_s = (f_s + 2)/f_s$ and the constant-volume heat capacity $c_{v,s}$ is computed from the maximum atomic heat capacity of hydrogen $R_{\rm H} \approx 8.3144 \times 10^7$ erg K^{-1} mole^{-1} via $c_{v,s} = \frac{1}{2} f_s R_{\rm H}/\mu_s$, where μ_s is the mass of the species in amu $= 1.66054 \times 10^{-24}$ g. We keep γ_s and $c_{v,s}$ constant for all species throughout the simulations presented in this work. Furthermore, Q_s and Q'_s encode the sources and sinks of mass and momentum for each species, while Γ_s encodes the heating and cooling. The exchange of momentum and energy due to collisions are given by (Schunk 1977; Schunk & Nagy 1980)

$$\frac{\mathrm{d}\mathcal{M}_s}{\mathrm{d}t} = \rho_s \textstyle\sum_{s'} \alpha_{ss'}(u_{s'} - u_s) \quad (4)$$

$$\frac{\mathrm{d}\mathcal{E}_s}{\mathrm{d}t} = \rho_s \textstyle\sum_{s'} \frac{\alpha_{ss'}}{m_s + m_{s'}} \left[m_{s'}(u_{s'} - u_s)^2 + 3k_{\rm B}(T_{s'} - T_s)\right]. \quad (5)$$

Here, m_s is the mass of the species s in g, the species temperature is T_s and k_B is the Boltzmann constant. Momentum conservation requires that the collision frequencies, $\alpha_{ss'}$, obey $\rho_s \alpha_{ss'} = \rho_{s'} \alpha_{s's}$. The first term in equation (5) is simply the energy generated by drag heating, while the second is the internal energy exchanged in collisions. We note that the drag terms conserve energy, i.e. $\sum_s u_s \frac{\mathrm{d}\mathcal{M}_s}{\mathrm{d}t} + \frac{\mathrm{d}\mathcal{E}_s}{\mathrm{d}t} = 0$. We leave the differential operator, $\nabla\cdot$, unspecified in terms of coordinate system, as we implemented cartesian, cylindric, and spherical coordinates. The cartesian coordinate system can be handily used to perform numerical tests, e.g. shock tube tests.

Optionally, we couple these equations with the equations of radiation transport. AIOLOS treats radiation transport using a multiband version (Vaytet et al. 2013) of the hybrid flux-limited diffusion approximation (Kuiper et al. 2010; Commercon et al. 2011; Bitsch et al. 2013). In practice this means that the incoming and potentially ionizing stellar irradiation is solved for by direct ray-tracing in plane-parallel geometry, whereas the exchange of thermal energy between gas and photons is solved via the flux-limited diffusion approximation (Levermore & Pomraning 1981) in spherical geometry. When the radiation module is activated, we compute

$$\Gamma_s = \sum_b^{\text{bands}} \rho_s \kappa^b_{\mathrm{P},s} \left[4\pi J^b - f^b(T_s) 4\sigma_{SB} T_s^4\right] + \Delta S_s + \Lambda_s, \quad (6)$$

where $\sigma_{SB} = 5.67 \times 10^{-5}$ erg s^{-1} cm^{-2} K^{-4} is the Stefan–Boltzmann radiation constant, J^b is mean photon intensity in the band, b, $\kappa^b_{\mathrm{P},s}$ is the Planck-mean opacity of species s averaged over the band b and $f^b(T_s)$ is the fraction of the total blackbody radiation at T_s that is emitted into each band. In the hybrid method, which is the default setting, the direct heating from the stellar radiation for species s is ΔS_s and high-energy cooling as well as non-thermal cooling from collisions with free electrons Λ_s (which we call high-energy cooling), is included in the energy equation as stated above. This approach is chosen rather than solving a two-stream system for the radiation due to its relative simplicity. Since AIOLOS is a 1D code, we treat the stellar irradiation in the surface-averaged approximation (e.g. Guillot 2010), where the exact local expression becomes (Mellema et al. 2006):

$$\Delta S_s = \tfrac{1}{4} \int \frac{S^{\odot}(\nu)}{h\nu} \exp(-\tau_{\odot}(\nu)) \rho_s \kappa_{\odot,s}(\nu) \mathrm{d}\nu \quad (7)$$

$$\approx \tfrac{1}{4} \textstyle\sum_b^{\text{bands}} S^{\odot,\,b} \exp(-\tau^b_{\odot}) \rho_s \kappa^b_{\odot,s}, \quad (8)$$

where the factor 1/4 results from the ratio of geometric planetary absorption cross-section to total planetary surface, over which the absorbed energy is distributed. Furthermore, $\tau^b_{\odot}$ is the total optical depth to the stellar radiation computed from the Planck-mean opacity to stellar radiation in the b-band $\sum_s \kappa^b_{\odot,s}$ and $S^{\odot,\,b}$ is the stellar flux at $\tau^b = 0$, and the energies of stellar photons at frequency ν are

$h\nu$. In practice, the frequency dependence is absorbed into a finite number of bands. In the cases where ionizing radiation can change the density ρ_s, the optical depth and ionization rate have to be solved for simultaneously, we describe this process in Section 3.4. The mean intensity of the photon field, J^b, obeys the time-dependent equation

$$\frac{1}{c}\frac{\partial J^b}{\partial t} + \frac{1}{4\pi}\nabla \cdot F^b = -\sum_s^{\text{species}} \rho_s \kappa_s^b \left[J^b - f^b(T_s)\frac{\sigma_{SB}}{\pi}T_s^4\right], \tag{9}$$

where the photon flux F^b is computed in the flux-limited diffusion approximation:

$$F^b = -\frac{4\pi\lambda(J^b)}{\sum_s \rho_s \kappa_s^b}\nabla J^b. \tag{10}$$

For the flux limiter, $\lambda(J_b)$ (Levermore & Pomraning 1981), we use the version given by Kley (1989).

$$\lambda(J) \equiv \lambda(R) = \begin{cases} \frac{2}{3+\sqrt{9+10R^2}} & R \leq 2 \\ \frac{10}{10R+9+\sqrt{81+180R}} & R > 2 \end{cases}, \tag{11}$$

where the photon mean-free path parameter, R, is

$$R = \frac{\xi}{\sum_s \rho_s \kappa_s^b}\frac{|\nabla J|}{J}. \tag{12}$$

Generally, it is $\lambda(R \to 0) = \frac{1}{3}$ (optically thick) and $\lambda(R \to \infty) = \frac{1}{R}$ (optically thin). The purpose of the flux limiter is to regularize the flux in optically thin regions, where without it the diffusion approximation would produce radiation that travels faster than the speed of light. With the flux limiter included the maximum flux obtained is $|F^b| = 4\pi J/\xi = cE_R/\xi$, where E_R is the volumetric energy density of radiation. In other words, for the standard choice, $\xi = 1$, the maximum speed at which the radiation energy is transported is the speed of light. The parameter $\xi = 1$ is, however, just a choice, and any value of $\xi \geq 1$ would obey causality while also producing the correct behaviour in the optically thick regime (where the flux is independent of R).

As we will show later, $\xi = 1$ may not be the best choice for planet evaporation models. The reason behind this is that the optical depth can vary rapidly on length-scales smaller than the planet's radius. In such a case, the atmosphere can be well modelled by a plane-parallel slab, for which $H = F/4\pi = J/2$ is a good approximation for the flux in the optically thin regions (e.g. Guillot 2010). Hence, $\xi = 2$ seems natural for planetary atmosphere applications. That $\xi > 1$ holds in a plane-parallel atmosphere is evident from the fact there is always a significant flux of radiation in the close-to horizontal directions so the average flux of radiation away from the planet must be less than the maximal case, in which all of the radiation is travelling directly away from the planet. However, far from the planet the radiation will seem as if it is emitted from a point source, and in such a case it is straight forward to verify that $\xi = 1$ is appropriate. This makes it clear that ξ (or more directly, the Eddington tensor) must vary with radius. Although this can be accounted for, e.g. in a variable Eddington tensor method, we simply note that while $\xi = 1$ may be favourable for some problems it is sensible to allow users to choose the value of ξ that best suits their problem. We highlight the physical effects of the choice of ξ in Section 6.

3 NUMERICAL METHODS

We solve equations (1)–(3) and (9) using a finite-volume approach. The spatial domain is discretized into a series of cells on a fixed grid. Each cell, with the numbering i starting at 0, is specified by its cell centre, r_i, and edges, $r_{i-1/2}$ and $r_{i+1/2}$, which have corresponding surface areas $A_{i-1/2}$ and volumes V_i. We denote by $\boldsymbol{U}^n_{s,i} = \{\rho_{s,i}, \rho_{s,i}u_{s,i}, E_{s,i}\}$ and $J^n_{b,i}$ the average of the conserved fluid variables and mean-intensity of radiation over the volume of cell i at time t_n, respectively. Fig. 1 illustrates the work flow of the program in a global overview. Details on the individual substeps are presented in the following sections. All substeps are solved via simple operator-splitting (Stone & Norman 1992) in order to construct a full solution after one time-step. As shown in Fig. 1, the code first reads in the initial parameters in order to construct the initial conditions $\boldsymbol{U}^n_{s,i}$ per species.

In our file structure, ∗.par files contain global simulation parameters, ∗.spc files are a list of all species properties, such as m_s, f_s, relative initial amount, which contain further links to opacity files.

The initial conditions for both evaporation and accretion problems require first a guess of the temperature profile, adiabatic or isothermal by default, from which a hydrostatic density profile is constructed in the given gravitational potential using the species data from the input files. The code then begins the main loop, evolving the system of equations. This consists of the hydrodynamic subloop, which evolves each species separately first and then secondly couples their velocities, in case the friction flag is set. After the hydrodynamic part, first the opacities are calculated per species, based on the given density and temperature. This results in knowledge of the optical depths. In the case that the incoming radiation is ionizing, optical depth and ionization rates need to be self-consistently computed in the ionization routine. Once the optical depths are self-consistent, the heating function can be computed from the optical depth per cell. With the heating function per cell known, the radiation transport step is finally solved, updating all species' temperatures and the thermal radiation fields. The code performs a positivity check of important quantities such as ρ_s, p_s, and T_s and advances to the next time-step if the check is passed, it stops the simulation otherwise. We now move to describe each of the individual steps in greater detail.

3.1 The hydrodynamic substep

The hydrodynamics module solves the sub-system

$$\frac{\partial \boldsymbol{U}_s}{\partial t} + \nabla \boldsymbol{F}_s = \boldsymbol{G}_s, \tag{13}$$

where

$$\boldsymbol{F}_s = \left\{\rho_s u_s,\ \rho_s u_s^2 + p_s,\ u_s(E_s + p_s)\right\} \tag{14}$$

$$\boldsymbol{G}_s = \{0,\ -\rho_s \nabla\Phi,\ -\rho_s u_s \nabla\Phi_s\} \tag{15}$$

using the well-balanced Godunov method of KM16. In this approach, the conserved variables are updated according to

$$\boldsymbol{U}^{n+1}_{s,i} = \boldsymbol{U}^n_{s,i} + \mathcal{L}_{\mathcal{H},i}(\boldsymbol{U}^n_s)\Delta t \tag{16}$$

$$= \boldsymbol{U}^n_{s,i} - \Delta t \frac{\left[A_{i+1/2}\boldsymbol{F}^n_{s,i+1/2} - A_{i-1/2}\boldsymbol{F}^n_{s,i-1/2}\right]}{V_i} + \tilde{\boldsymbol{G}}^n_{s,i}. \tag{17}$$

The interface fluxes, $\boldsymbol{F}^n_{s,i-1/2} \equiv \boldsymbol{F}(\boldsymbol{W}^n_{\mathrm{L},s,i-1/2}, \boldsymbol{W}^n_{\mathrm{R},s,i-1/2})$ are obtained from the primitive variables ($\boldsymbol{W}_s = \{\rho_s,\ u_s,\ p_s\}$) evaluated at the left and right side of the interface using the HLLC Riemann Solver (Toro et al. 1994). This solver shows exceptional behaviour in the standard shock tube tests (Toro 2009) and is particularly well-suited to be used in conjunction with the well-balancing as presented by KM16, as it reproduces standing and slow-moving contact waves particularly well. On a uniform grid given by a coordinate x, the method proposed by KM16 becomes a reconstruction which satisfies

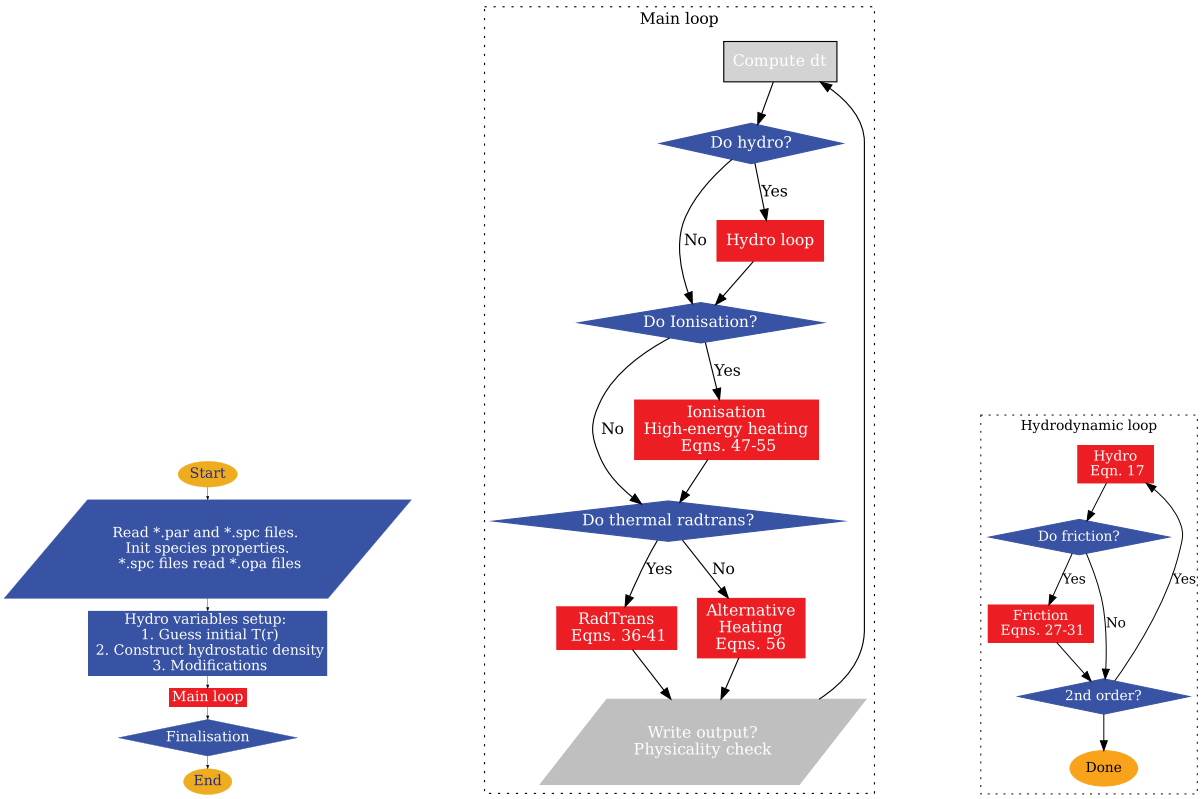

Figure 1. Flow charts to illustrate the data flow in AIOLOS. All modules (hydrodynamic, friction, ionization, and radiation transport) can be switched on and off, allowing for different physical approximations to be realized in the main program loop, such as hydrostatic radiation transport or hydrodynamic isothermal runs.

the relation

$$-\frac{\left[p^n_{s,i+1/2}-p^n_{s,i-1/2}\right]}{\Delta x}+\frac{\rho^n_{s,i}+\rho^n_{s,i+1}}{2}\frac{\Phi_{i+1}-\Phi_i}{\Delta x}=0. \tag{18}$$

This can be achieved by extrapolating the cell centred pressures to the interfaces via

$$p^n_{s,i}(x_{i\pm1/2})=p^n_{s,i}+\rho^n_{s,i}\frac{\phi_i-\phi_{i\pm1}}{2}, \tag{19}$$

and using and $\boldsymbol{W}_{\mathrm{R},s,i-1/2}=\{\rho_{s,i},u_{s,i},p_i(x_{i-1/2})\}$.

These expressions can be generalized to non-uniform, non-cartesian grids and second-order spatial reconstructions as described in KM16 – it is these generalizations, together with the monotonized-central slope limiter from Mignone (2014), that we use in the code.

The source term $\tilde{\boldsymbol{G}}_{s,i}$ includes the gravitational source term and an additional $-2\,p\,/\,r$ correction (in spherical symmetry) that appears when pulling $\partial P/\partial r$ into the differential operator in conservative form. The source term must be computed carefully to ensure that hydrostatic equilibrium is properly maintained, which we do via

$$\tilde{\boldsymbol{G}}_{s,i}=-\begin{bmatrix}0\\ \rho_{s,i}\\ u_{s,i}\rho_{s,i}\end{bmatrix}\left.\frac{\partial\Phi}{\partial r}\right|_i+a_{\mathrm{R},i}\begin{bmatrix}0\\ p^*_{i+1/2}\\ 0\end{bmatrix}-a_{\mathrm{L},i}\begin{bmatrix}0\\ p^*_{i-1/2}\\ 0\end{bmatrix}, \tag{20}$$

where $p^*_{i\pm1/2}$ is the pressure at the interface returned by the Riemann Solver and $\left.\frac{\partial\Phi}{\partial r}\right|_i$ is computed as in appendix A of KM16. The factors $a_{\mathrm{L/R},i}$ are essentially the difference between $\frac{1}{r^2}\frac{\partial r^2P}{\partial r}$ and $\frac{\mathrm{d}P}{\mathrm{d}r}$, i.e.

$$a_{\mathrm{R},i}=\frac{A_{i+1/2}}{V_i}-\frac{1}{r_{i+1/2}-r_{i-1/2}} \tag{21}$$

$$a_{\mathrm{L},i}=\frac{A_{i-1/2}}{V_i}-\frac{1}{r_{i+1/2}-r_{i-1/2}}. \tag{22}$$

To achieve second-order accuracy in time, we use the strong stability preserving (SSP) Runge–Kutta time-stepping scheme (Gottlieb, Shu & Tadmor 2001):

$$\boldsymbol{U}^*_{s,i}=\boldsymbol{U}^n_{s,i}+\mathcal{L}_{\mathcal{H},i}(\boldsymbol{U}^n_s)\Delta t, \tag{23}$$

$$\boldsymbol{U}^{n+1}_{s,i}=\boldsymbol{U}^n_{s,i}+\tfrac{1}{2}\left[\mathcal{L}_{\mathcal{H},i}(\boldsymbol{U}^n_s)+\mathcal{L}_{\mathcal{H},i}(\boldsymbol{U}^*_s)\right]\Delta t. \tag{24}$$

Note that we also apply the friction and collisional heat exchange terms to $\boldsymbol{U}^*_{s,i}$ before evaluating the second step (equation 24).

3.2 The friction and collisional heat exchange substeps

In the friction step, we solve the subsystem

$$\frac{\partial\rho_s u_s}{\partial t}=\rho_s\textstyle\sum_{s'}\alpha_{ss'}(u_{s'}-u_s). \tag{25}$$

$$\frac{\partial\rho_s e_s}{\partial t}=\rho_s\textstyle\sum_{s'}\frac{\alpha_{ss'}m_{s'}}{m_s+m_{s'}}(u_{s'}-u_s)^2. \tag{26}$$

Since $\alpha_{ss'}\propto\rho'_{s'}$ the drag term can be large in dense regions of the atmosphere and the friction step can be very stiff. Therefore we solve for the new velocity using a semi-implicit method in which $\alpha_{ss'}$ is evaluated at t_n, whereas u_s is evaluated at t_{n+1}

$$\frac{u^{n+1}_{s,i}-u^n_{s,i}}{\Delta t}=\sum_{s'}\alpha^n_{ss',i}\left(u^{n+1}_{s',i}-u^{n+1}_{s,i}\right) \tag{27}$$

and ρ_s is held constant. We assume here that $\alpha_{ss'}$ is constant over the time-step, an approximation which has been shown by Benítez-Llambay et al. (2019) to be acceptable. This is a linear system of equations coupling the velocities of all species in cell i, which we

solve using the EIGEN linear algebra package. Similar approaches to treating drag forces were taken by Toth (1995), Stone (1997), and Benítez-Llambay, Krapp & Pessah (2019).

Since energy is conserved under the action of drag forces, it is important to evaluate equation (26) in such a way that the numerical scheme also conserves energy. To achieve this we use the fact that the change in kinetic energy of two species s and s' arising due to the interaction between these species should only heat those two species. Taking the force due to the interaction of species s with s' to be $\rho_s \alpha^n_{ss',i}(u^{n+1}_{s',i} - u^{n+1}_{s,i})$ for consistency with equation (27), the contribution to the change in kinetic energy of s by this interaction during the time-step is

$$W_{ss',i} = \Delta t \rho_{s,i} \alpha^n_{ss',i} \left(u^{n+1}_{s',i} - u^{n+1}_{s,i}\right) \frac{\left(u^n_{s,i} + u^{n+1}_{s,i}\right)}{2} \tag{28}$$

and $W_{s's,i}$ follows by symmetry.

Since the change in $e_{s,i}$ and $e_{s',i}$ due to the drag force acting between them should equal $W_{ss',i} + W_{s's,i}$, this implies the following form for the energy update,

$$\begin{aligned}(\rho e)^{n+1}_{s,i} &= (\rho e)^n_{s,i} \\ &+ \Delta t \rho^n_{s,i} \sum_{s'} \frac{\alpha^n_{ss',i} m_{s'}}{m_s + m_{s'}} \left(u^{n+1}_{s',i} - u^{n+1}_{s,i}\right) \left(u^{n+1/2}_{s',i} - u^{n+1/2}_{s,i}\right),\end{aligned} \tag{29}$$

where $u^{n+1/2}_{s,i} = (u^n_{s,i} + u^{n+1}_{s,i})/2$. We then set $E^{n+1}_{s,i} = \frac{1}{2}\rho^n_{s,i}(u^{n+1}_{s,i})^2 + (\rho e)^{n+1}_{s,i}$. It is straightforward to verify that equations (27) and (29) together conserve energy by comparing $\sum_s E^n_{s,i}$ and $\sum_s E^{n+1}_{s,i}$.

We treat the collisional heat exchange term,

$$\frac{\partial E_s}{\partial t} = \rho_s \sum_{s'} \frac{\alpha_{ss'}}{m_s + m_{s'}} 3 k_{\rm B} (T_{s'} - T_s), \tag{30}$$

in an analogous way. By holding ρ_s, $\alpha_{ss'}$, and u_s constant we can write

$$c_{v,s} \frac{T^{n+1}_{s,i} - T^n_{s,i}}{\Delta t} = \sum_{s'} \frac{\alpha^n_{ss',i}}{m_s + m_{s'}} 3 k_{\rm B} \left(T^{n+1}_{s',i} - T^{n+1}_{s,i}\right), \tag{31}$$

In cases where we neglect radiation transport we again solve this linear equation using the EIGEN linear algebra package. When radiation transport is modelled we instead include this term in the radiation substep (equation 43).

3.3 The thermal radiation transport substep

3.3.1 Opacities and stellar absorption

Before going into details of the radiation transport solver, we reiterate the definitions of three customarily used mean-opacities. Given a wavelength-resolved opacity function $\kappa_\nu(\rho, T)$, one can define the Rosseland-mean κ_R as

$$\kappa_R^{-1}(\rho, T) = \frac{\int_0^\infty {\rm d}\nu\, \kappa_\nu^{-1}(\rho, T) \partial_T B_\nu(T)}{\int_0^\infty {\rm d}\nu \partial_T B_\nu(T)}, \tag{32}$$

where $B_\nu(T)$ is the Planck-function as function of temperature. The single-temperature Planck-mean is

$$\kappa_{\rm P}(\rho, T) = \frac{\int_0^\infty {\rm d}\nu\, \kappa_\nu(\rho, T)\, B_\nu(T)}{\int_0^\infty {\rm d}\nu B_\nu(T)} \tag{33}$$

and the two-temperature Planck-mean or stellar opacity, which additionally depends on the structure of the irradiating field, given by the stellar blackbody at $T_\odot$, is

$$\kappa_\odot(\rho, T, T_\odot) = \frac{\int_0^\infty {\rm d}\nu\, \kappa_\nu(\rho, T)\, B_\nu(T_\odot)}{\int_0^\infty B_\nu(T_\odot)}. \tag{34}$$

Note that with those definitions, it is κ_R that determines whether a cell is optically thin or thick towards its own radiation, furthermore it is $\kappa_{\rm P}$ which locally couples the gas internal energy equation with the radiative energy equation, and $\kappa_\odot$ determines the stellar absorption in the ΔS-terms. Values for these three types of opacities can be found tabulated for gas-mixtures relevant to planet formation in Freedman et al. (2014) and Malygin et al. (2014) as functions of ρ, T, and $T_\odot$, but for the sake of simplicity we use $\kappa_{\rm P} = \kappa_R \neq \kappa_\odot$ not being functions ρ, T, and $T_\odot$ in this paper. We stress, however, that in future applications, with gases at arbitrary mixing ratios of species, it is necessary to know the per-species contributions to those opacities. As the attenuation of stellar radiation per cell is non-linear with their contributions w.r.t individual species' opacities, one has to take an indirect approach in order to compute the amount of stellar heating per species. First, the stellar radiation reaching cell wall $i + 1/2$ is computed from determining the total attenuation due to the opacities of all species in band b,

$$S^b_i = S^{\odot,\,b} \cdot exp\left(-\tau^b_{\odot,i}\right), \tag{35}$$

with the total optical depth until the cell boundary

$$\tau^b_{\odot,i} = \int_\infty^{r_{i+1/2}} dr \sum_s^{\rm species} \rho_{s,i} \kappa^b_{\odot,s,i} \tag{36}$$

with the dr appropriately chosen, and between the cell walls it is

$$\Delta\tau^b_{\odot,i} = \Delta r \sum_s^{\rm species} \rho_{s,i} \kappa^b_{\odot,s,i} \tag{37}$$

The attenuation of radiation, i.e. the total photon energy deposited inside a cell is

$$\Delta S^b_i = \frac{1}{4} \frac{\partial S^b_i}{\partial r}(r_i) \approx \frac{1}{4} S^b_i \frac{1 - \exp\left(\Delta\tau^b_{\odot,i}\right)}{\Delta r}. \tag{38}$$

The latter is the cell-average of the local quantities in equation (8), (see also Mellema et al. 2006) and the correct form for both non-ionizing and ionizing radiation. The complication for ionizing radiation is that in between computing the opacities and the optical depths, one needs to find the density self-consistently with the given ionization rates. This is described in more detail in the following sections. In the cases for which we consider optically thick heating of the atmosphere from the planetary surface, we model a the internal planetary heat flux $\sigma T^4_{\rm int}$ by depositing the energy in the first active cell of size Δr, resulting in an additional contribution to the heating in this cell of

$$\Delta S^b_0 \mathrel{+}= \frac{\sigma T^4_{\rm int}}{\Delta r}. \tag{39}$$

Alternatively, this is implemented as a radiative flux $F = \sigma T^4_{\rm int}$ at the inner boundary. Next, the heating per species in this band and cell is reconstructed in a manner that conserves the photon number, via its fractional contribution to the total optical depth for a given cell and band, as

$$\Delta S^b_{s,i} = \Delta S^b_i \times \frac{\rho_{s,i} \kappa^b_{\odot,s,i}}{\sum_s \rho_{s,i} \kappa^b_{\odot,s,i}}. \tag{40}$$

Finally, the total stellar heating $\Delta S_{s,i}$ for a species in a given cell, which is required to solve each species' temperature equation, is

computed as the sum over all its band heating contributions, i.e.

$$\Delta S_{s,i} = \sum_{b}^{\text{bands}} \Delta S^{b}_{s,i}. \tag{41}$$

Note that we have omitted the time indices n here, as those operations all happen at the same time-step. The optical depths for ionizing radiation are computed in the same way, but have to be solved self-consistently with the change in a species' number density. Ionizing heating terms are furthermore assigned to their product species, after being computed on the basis of their reactant species' number densities (e.g. the reaction $\mathrm{H} + \mathrm{h}\nu \rightarrow \mathrm{H}^+ + \mathrm{e}^-$, will have its heating rate proportional to $\kappa_{\mathrm{H}}\rho_{\mathrm{H}}$, but the resulting heating rate must be split among H^+ and e^-). This is described further in the section on ionizing radiation. Once the opacities and heating source terms are known, one can proceed to the solution of the energy equations.

3.3.2 The thermal radiation solver

The radiation transport substep updates the internal energy density and mean radiative energy simultaneously. As radiative evolution time-scales can be shorter to any interesting hydrodynamic ones by many orders of magnitude, we use an implicit solution method. Both the J^b and T_s variables have to be evaluated at the advanced time-step $n+1$ for energy to be exactly conserved. In our implementation, however, opacities and stellar source function are taken at the retarded time-step, n. In our test problems this seems to be sufficient for reasonable numerical stability, and in fact even in the literature with non-constant opacities (Kuiper et al. 2010; Vaytet et al. 2012; Bitsch et al. 2013) this does not seem to be a problem as long as the opacity is not a strong function of the temperature. Additionally, we include the collisional heat-exchange terms in the internal energy update part of the radiation solver rather than solving for them separately via equation (31).

The internal energy part of the total energy equation is thus

$$\frac{\partial \rho_s e_s}{\partial t} = \Gamma_s + \rho_s \sum_{s'} \frac{\alpha_{ss'}}{m_s + m_{s'}} 3k_{\mathrm{B}}(T_{s'} - T_s), \tag{42}$$

which is solved simultaneously with equation (9) for the mean radiation intensity. For the solution of the radiation transport problem, we use the temperature form of the internal energy equation, found via $e_s = c_{v,s} T_s$, which then is

$$\begin{aligned} c_{v,s}\frac{T^{n+1}_{s,i} - T^{n}_{s,i}}{\Delta t} &= 4\pi \sum_{b}^{\text{bands}} \kappa^{b,n}_{\mathrm{P},s,i}\left[J^{b,n+1}_i - f^b(T^n_{s,i})B\left(T^{n+1}_{s,i}\right)\right] \\ &+ \frac{\Delta S^n_{s,i}}{\rho^n_{s,i}} + \sum_{s'} \frac{\alpha^n_{ss',i}}{m_s + m_{s'}} 3k_{\mathrm{B}}\left(T^{n+1}_{s',i} - T^{n+1}_{s,i}\right), \end{aligned} \tag{43}$$

where the mean intensity relates to the energy density via, $4\pi J = c\, E_{\mathrm{rad}}$ and $B(T) = \sigma T^4/\pi$. To solve this equation we linearize the $B(T)$ term following the approach of Commercon et al. (2011), i.e. $(T^{n+1}_{s,i})^4 = 4T^{n+1}_{s,i}(T^n_{s,i})^3 - 3(T^n_{s,i})^4$. The fraction $f^b(T_s)$ is tabulated at the beginning of each simulation using the Planck-integral and is fixed for the chosen band structure, from 10^{-10} to 10^{10} K. Since $\sum_b f_b(T) = 1$ for all temperatures, this guarantees energy conservation.

The discretized form of equation (9) is

$$\begin{aligned} &\frac{1}{c}\frac{J^{b,n+1}_i - J^{b,n}_i}{\Delta t} + \frac{1}{4\pi}\frac{\left[A_{i+1/2}F^{b,n+1}_{i+1/2} - A_{i-1/2}F^{b,n+1}_{i-1/2}\right]}{V_i} \\ &= -\sum_{s}^{\text{species}} \rho^n_{s,i}\kappa^{b,n}_{\mathrm{P},s,i}\left[J^{b,n+1}_i - f^b(T_s)B\left(T^{b,n+1}_{s,i}\right)\right], \end{aligned} \tag{44}$$

where the closure relation for relating fluxes and mean energy density is the discrete flux-limited diffusion relation

$$F^{b,n+1}_{i-1/2} = -\frac{4\pi\lambda(\overline{R}^{b,n}_{i-1/2})}{\overline{\rho\kappa_{\mathrm{R}}}^{b,n}_{i-1/2}}\left(\frac{J^{b,n+1}_{i-1} - J^{b,n+1}_i}{r_{i-1} - r_i}\right), \tag{45}$$

where the mass-weighted average Rosseland opacity between two cells is taken as $\overline{\rho\kappa_{\mathrm{R}}}^{b,n}_{i-1/2} = (\rho\kappa^{b,n}_{\mathrm{R},i-1} + \rho\kappa^{b,n}_{\mathrm{R},i})/2$. The average photon-mean free path parameter in the flux-limiter, $\overline{R}^{b,n}_{i-1/2}$, is defined by equation (12) and is approximated using the mass-weighted average Rosseland opacity via

$$\overline{R}^{b,n}_{i-1/2} = \frac{\xi}{\overline{\rho\kappa_{\mathrm{R}}}^{b,n}_{i-1/2}}\frac{J^{b,n}_{i-1} - J^{b,n}_i}{J^{b,n}_{i-1}} \tag{46}$$

which is sensible as long as the radiative flux vector is pointing away from the planet. The latter expression can be easily generalized via a standard upwinding method. Again, we refer to Section 6 to a discussion of the factor ξ. Equation (44) together with equation (43) form a block-tridiagonal system of linear equations (i.e. an $N_{\mathrm{cells}} \times N_{\mathrm{cells}}$ matrix of blocks with size $N_{\mathrm{species}} + N_{\mathrm{bands}}$). We solve these directly using the EIGEN linear algebra package to obtain the new temperatures and mean intensities.

3.4 The photoionization substep

We have implemented a flexible model for the ionization of multiple species, and use the process $H + \gamma \rightarrow \mathrm{p}^+ + \mathrm{e}^-$, (i.e. a simple two-system model, no atomic level populations are solved for in the current state of the code) as a simple test model for the source and sink terms, Q_{s} and Q'_{s}. Explicitly we include photoionization, collisional ionization, and recombination, along with the associated heating, cooling, and momentum exchange between the species. The net production/loss of hydrogen is given by

$$Q_{\mathrm{H}} = m_{\mathrm{H}}\frac{\partial n_{\mathrm{H}}}{\partial t} = m_{\mathrm{H}}\left\{\alpha_{\mathrm{HI}}(T_{\mathrm{e}})\, n_{\mathrm{e}} n_{\mathrm{p}} - [C_{\mathrm{HI}}(T_{\mathrm{e}})\, n_{\mathrm{e}} + \Gamma_{\mathrm{HI}}]\, n_{\mathrm{H}}\right\}, \tag{47}$$

where n_s is the number density of species, s, $\alpha_{\mathrm{H1}}(T_{\mathrm{e}})$ is radiative recombination coefficient and $C_{\mathrm{H1}}(T_{\mathrm{e}})$ is the collisional ionization coefficient. The photoionization rate is computed according to

$$\Gamma_{HI} = \frac{\partial S^b_i}{\partial r}(r_i) \approx S^{\odot,b} \cdot exp\left(-\tau^b_{\odot,i}\right)\frac{1 - \exp\left(\Delta\tau^b_{\odot,i}\right)}{\Delta r}. \tag{48}$$

Here, $S^{\odot,b}$ and S^b_i are the fluxes in any band b which is designated by the user to be ionizing. We use the fits to the Case B recombination rates from Hui & Gnedin (1997). This approximation corresponds to the'on-the-spot'-approximation, for which ground-state recombination photons are locally re-absorbed and do not further change the ionization rates (Mellema et al. 2006). The source terms for protons and electrons are given by $\frac{\partial n_{\mathrm{p}}}{\partial t} = \frac{\partial n_{\mathrm{e}}}{\partial t} = -\frac{\partial n_{\mathrm{H}}}{\partial t}$. To solve the above equations, we follow the C2-ray approach (Mellema et al. 2006; Friedrich et al. 2012), in which n_{e} and Γ_{H1} in equation (47) are replaced by their averages over the time-step. This ensures that the number of photons absorbed in the cell for heating is identical to the number of atoms that are photoionized. The resulting equations are

implicit in n_e, and are solved iteratively using the Brent method (e.g. Press et al. 2002).

Once the new densities have been determined, the next step is to compute the momentum and energy exchange due to photoionization. Applying momentum conservation to each of the processes individually implies that

$$Q'_H = \dot{n}_R(m_e v_e + m_p v_p) - \dot{n}_I m_H v_H \quad (49)$$

$$Q'_p = \dot{n}_I \frac{m_H v_H}{1+m_e/m_p} - \dot{n}_R m_p v_p \quad (50)$$

$$Q'_e = \dot{n}_I \frac{m_H v_H}{1+m_p/m_e} - \dot{n}_R m_e v_e, \quad (51)$$

where $\dot{n}_R = \alpha_{HI}(T_e)\, n_e n_p$ and $\dot{n}_I = [C_{HI}(T_e)\, n_e + \Gamma_{HI}]\, n_H$. We update the resulting change in momentum implicitly, i.e. via

$$m_H \frac{n_H^{n+1} v_H^{n+1} - n_H^n v_H^n}{\Delta t} = \dot{n}_R \left(m_e v_e^{n+1} + m_p v_p^{n+1} \right) - \dot{n}_I m_H v_H^{n+1}, \quad (52)$$

where $\dot{n}_R$ and $\dot{n}_I$ are replaced with the time-averaged rates computed in the first step of the photoionization routine. Similarly n_H^n and n_H^{n+1} are the number density before and after the first step in the photoionization calculation. This equation can be solved along with the equivalent expressions for the other species to determine the new velocities, v_s^{n+1}.

Now that the new density and velocity of each species has been computed we can evaluate the total change in kinetic energy, ΔE_k. To ensure energy conservation we add this to the internal energy of the protons and electrons in the proportions $1/(1 + m_p/m_e)$ and $1/(1 + m_e/m_p)$, respectively.

Finally, the heating and cooling due to photoionization are given by

$$\Lambda_H = \dot{n}_R m_p C_p T_p - \dot{n}_I m_H C_H T_H \quad (53)$$

$$\Lambda_p = \dot{n}_I \left(\frac{m_H C_H T_H}{1+m_e/m_p} + \frac{E_{HI}}{1+m_p/m_e} \right) - \dot{n}_R m_p C_p T_p \quad (54)$$

$$\Lambda_e = \dot{n}_I \left(\frac{m_H C_H T_H}{1+m_p/m_e} + \frac{E_{HI}}{1+m_e/m_p} \right) - \Lambda(T_e). \quad (55)$$

The terms related to ionization (proportional to $\dot{n}_I$) can be derived by considering energy and momentum conservation during ionization, where E_{HI} is the average energy injected per ionization. This middle term is the high-energy equivalent of equation (41). To prevent double counting of photons in cases of mixed ionizing and non-ionizing absorption, we keep track of the high-energy optical depth separately and substract it from the non-high energy photons, individually per band, per cell, to obtain the correct heating rates.

During recombination, the excess kinetic energy is lost to radiation. We have assumed this energy comes entirely from the electrons due to their higher velocities.[2] It can be verified by summing the three terms that the net heating rate is just the energy injected per ionization minus the total cooling. Note that $\Lambda(T_e)$ is the total cooling rate, including recombination cooling and Lyman-alpha cooling (which is important for atmospheric photoevaporation, Murray-Clay et al. 2009).

Since the heating and cooling rates can be numerically stiff when the ionization or recombination time-scales are short, we evaluate them semi-implicitly in the cases that thermal radiation transport is switched off in the code, by solving a modified version of equation (31), i.e.

$$c_{v,s} \frac{\rho_s^{n+1} T'_s - \rho_s^n T_s^n}{\Delta t} = \rho_s^{n+1} \sum_{s'} \frac{\alpha_{ss'}^n}{m_s + m_{s'}} 3k_B (T'_{s'} - T'_s) + \Lambda'_s, \quad (56)$$

where Λ'_s is evaluated using T'. This intermediate value of T' is then used to specify the heating and cooling rate used in the radiation transport substep. With now conclude our technical description of the solution algorithms and turn to show test results.

4 RESULTS – HYDROSTATICS AND HYDRODYNAMICS

In order to be able to reproduce the simulation test cases shown in this and the subsequent sections, we list the most important initial conditions in Table 2.

4.1 Hydrodynamic tests without gravity

We conducted basic hydrodynamic tests to make sure that the hydrodynamic solver works correctly. These include the seven standard shock-tube tests as given in Toro (2009), which we tested using a cartesian domain on $x \in [0, 1]$ with a resolution of 100 cells. We confirmed that the HLLC solver resolves all waves correctly, with the code reproducing analytical solution results and converging as one would expect for the first and second order solvers as the resolution is increased. We also checked that for injected single sound-waves, the solution converges appropriately to the chosen order as in Stone et al. (2008); second order for the method described here. Since all those results are standard in the literature, we merely confirmed the codes correct functionality, but do not present them here. These tests are run regularly as part of our standard test package, included on the git repository.

4.2 Hydrodynamics + gravity: well-balanced quasi-isothermal Parker winds

In this section, we report on the tests concerning the well-balancing against gravity and its usefulness for hydrodynamic outflow simulations.

As shown in KM16, any hydrostatic profile should remain stable if constructed to obey a specific discrete hydrostatic equilibrium. The density profile is constructed by inverting equation (18) for $\rho^n_{s,i+1}(\rho^n_{s,i})$. The simulation domain was chosen to be between $r \in [0.1, 100]R_s$, where R_s is the sonic radius. The boundary conditions employed are reflective at the inner radius and open boundaries with a hydrostatic pressure extrapolation at the outer boundary. We show the evolution of the velocity fluctuations, i.e. the differences to zero velocity, of an atmosphere in Fig. 2, (**left**) for the case of a quasi-isothermal gas giant. Note that the velocity fluctuations in this figure are up-scaled by a factor of 10^{10}. Further, the velocity fluctuations remain relatively static with the mach number $v/c_s \sim 10^{-13}$–10^{-15} over the entire simulation domain after 10 sound-crossing times.

Deep in the atmosphere, at $r/R_s < 0.1$ the hydrostatic equilibrium is kept extremely well, as can be seen in the small magnitude of the velocity in those profiles, with larger fluctuations at and above the sonic point. Some non-zero growth of the velocity noise in this region at $r/R_s > 1.0$ of the high atmosphere exists. Considering that this is however the region that is dynamically most active in realistic settings, this slight growth in velocity fluctuations should never play any significant role for applied, dynamic simulation cases.

[2]Note that a more sophisticated calculation of recombination cooling can only slightly change the partitioning of the recombination cooling between protons and electrons because the final energy of the neutral atoms formed is determined by energy conservation.

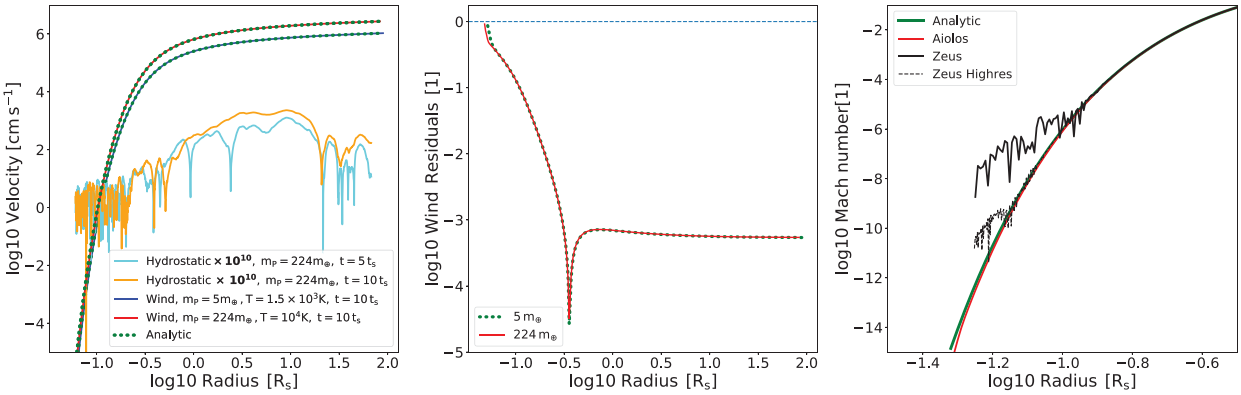

Figure 2. Effects of the well-balancing for quasi-isothermal simulations. All quantities are plotted as functions of the radius, in units of the isothermal sonic radius. We check the properties of the code to sustain an entirely hydrostatic solution over 10 t_s (**Left**). The velocity solution in the fully hydrostatic case has been scaled up by $\times$ 10^{10} and shows only numerical noise in its velocity fluctuations. Hydrodynamic wind solutions are shown for a hot Jupiter and a planet of drastically lower mass (**Left**). The residuals w.r.t the analytical wind solutions (**Middle**) for both planets are stable (identical for both masses) and better than 10^{-3} at the sonic radius. The thin, blue dashed line is added for reference of the unity level. The hot Jupiter wind is finally compared to a solution generated via ZEUS (Stone & Norman 1992) (**Right**). The simulations are shown at the same numerical resolution (solid lines) and one at double the resolution (dashed black line).

To highlight the robustness of the KM16-scheme we confirmed that other hydrostatic density profiles of arbitrary entropy stratification remain stable at the same levels of quality (not shown). Entropy stratifications tested were adiabatic (with $\gamma = 1.4$), quasi-isothermal (adiabatic with $\gamma = 1 + 10^{-8}$ for both masses of 5 $m_\oplus$ and 224 $m_\oplus$) and a 'bumpy' temperature profile consisting of arbitrarily strong temperature inversion on top of the adiabatic temperature, all giving the same order of magnitude of final mach numbers.

Next, we tested the quality of our hydrodynamic, quasi-isothermal solutions. The numerical solutions are contrasted with those computed by Parker (1965) (dubbed 'analytical'), with the formalism from Cranmer (2004) for a 5 $m_\oplus$ and a 224 $m_\oplus$ planet. The numerical wind solutions match the analytical solutions near perfectly (see Fig. 2, left) and that remains true for the low-mass planet when inspecting the residuals $1 - v_{\rm num}/v_{\rm ana}$ (see Fig. 2, middle). A clear increase in residuals due to the boundary condition, which forces $v = 0$, whereas the Parker wind remains with $v \neq 0$ for all radii, is evident as well. Note that we moved the inner simulation radius compared to the hydrostatic solutions to smaller radii (see Table 2), in order to emphasize the effects of the boundary on the residuals.

Lastly, to highlight the improvement of well-balanced schemes over more traditional numerical approaches, we contrast our solutions in the deep hydrostatic atmosphere with those produced by an identical setup in the ZEUS code (Stone & Norman 1992). The setup is inspired by Font et al. (2004), only adapted for 1D planetary atmospheres without the action of centrifugal and Coriolis terms. We again use a hot Jupiter-like exoplanet, an adiabatic, quasi-isothermal $\gamma_{\rm adi} = 1 + 10^{-8}$, the mean molecular mass $m_{\rm particle} = 2$ a.m.u., numerical resolution of 100 cells per decade after 10 t_s (solid black, solid red line) and at double resolution after 10^3 t_s (black dashed). Our well-balanced code compares excellent to the analytical solution by Cranmer (2004) and only a tiny systematic difference very deep in the atmosphere exists, again attributable to boundary condition effects. ZEUS on the other hand, as a non-well-balanced finite difference scheme, has larger trouble in finding the same magnitude of precision and systematics of velocity fluctuations.

5 RESULTS – FRICTION

For a purely isothermal gas mixutre, the coupling between multiple species is entirely given by their momentum exchange due to drag forces. Hence, to test the drag module included in our code, outlined in previous sections, we use a simple multiple-species-in-a-box approach, without the action of gravity, identical to the tests outlined in Benítez-Llambay et al. (2019). A further test, including the action of gravity, serves to test our numerical results against the subsonic two-species drag approximation of Zahnle & Kasting (1986; hereafter ZK86).

5.1 Drag without gravity

Here, we conducted tests to confirm that the evolution of multiple fluids uniform density, velocity, and pressure evolves as expected. The tests were identical to the one presented in Benítez-Llambay et al. (2019) and used 2, 3, or 6 species. We confirmed that our algorithm agrees with the analytical solutions for constant friction coefficients, $\alpha_{\rm ij}$. Energy and momentum are conserved to better than one part in 10^{10} after a frictional time. We also check for the attainment of the correct steady-state mean velocity $\bar{v}$

$$\bar{v} = \frac{\sum_s \rho_s v_s(t=0)}{\sum_s \rho_s}. \tag{57}$$

For the sake of brevity, we do not show these tests, as they would add nothing crucial to our presentation.

5.2 Drag including gravity – Fractionation

The effects of inclusion of gravity on a single species have already been discussed above. With the addition of more species, e.g. a trace species, the dominant force contribution on those species can shift from drag-dominated to gravity-dominated anywhere in the simulation domain. We show that in both those limits our code produces correct results, using two species with masses m_i, m_j and $m_j > m_i$. In this case, ZK86 have given approximate analytical results for the mass flux ratio at infinity. Furthermore, both in their work and here, non-constant collision coefficients of $\alpha_{ij} = k_{\rm B}Tn_j/(m_i b_{ij})$ and the experimentally measured $b_{ij} = 5 \times 10^{17} \times (T/300\ {\rm K})^{0.75}$ are employed. Those values are given in ZK86 for H_2–He collisions, but for reasons of simplicity we employ them for collisions with the no-name species as well. The two-species fractionation factor defined as $x_j \equiv \frac{n_i v_i}{n_j v_j}(R_s)\frac{n_j}{n_i}(r_{\rm base})$ i.e. the mass flux ratio at the sonic point, normalized to the density ratio at some base radius $r_{\rm base}$, which can

be different from the lower simulation boundary radius r_0, can be computed according to their approximate solution as

$$x_j = \frac{\mu\Phi_i - (\mu - 1)}{\mu\Phi_i - (\mu - 1)\exp\left[-\omega_0(\mu\Phi_i - (\mu - 1))\right]}, \tag{58}$$

where

$$\mu = m_j/m_i, \tag{59}$$

$$\Phi_i = \left(n_i r^2\right)|_{r=r_{max}} \frac{k_B T}{G m_p m_j b_{ij}}, \tag{60}$$

$$\omega_0 = \bar{r}_s/r_B, \tag{61}$$

$$\bar{r}_s = \frac{G m_p}{k_B T}\frac{m_i m_j}{m_i + m_j}. \tag{62}$$

We first compare the behaviour of the dragged solution for one simulation over the entire simulation domain. The results of this can be seen in Fig. 3. The left-hand and middle panel shows the behaviour of the mass-flux $4\pi\rho v r^2$ and the density for primary (H_2) and a secondary species (He). Those panels showcase the effect of chosing the right base radius for the comparison of numerical with the analytical solution, e.g. equation (58). When the time-dependent problem has not run into steady-state yet, chosing $r_{\rm base} = r_0$ as the inner boundary, can result in a faulty comparison. If one however computes $r_{\rm base}$ such that it corresponds to the flow time of the parcel over the passed simulation time, denoted as $r_{\rm base} = r_{\rm flow}$, one obtains much better agreement in mass-flux, density profile, and velocity differences, as shown in Fig. 3.

The velocity differences can be expressed in a generalization of equation (9) in ZK86 which gives,

$$u_i - u_j = \frac{k_B T\, n_j}{m_i n\, b_{ij}}\left[\frac{n}{n_i n_j}\frac{\partial n_i}{\partial r}\left(1 - \frac{n_i}{n}\right) - \frac{1}{n_j}\frac{\partial n_j}{\partial r} + \frac{m_j - m_i}{m_i + m_j}\frac{1}{p_i}\frac{\partial p_i}{\partial r} + \frac{g(m_j - m_i)}{k_B T}\right], \tag{63}$$

where $n = n_i + n_j$ and $p_i = p_{\rm H2}$ is the pressure of the mass-dominating species. The velocity differences from the simulation are then compared to the velocity difference that should arise from the simulations structure data plugged into equation (63). In Fig. 3, it can be seen that they achieve acceptable agreement. Given that equation (63) is itself derived via the hydrostatic approximation in ZK86, we however do not expect perfect agreement. We show in the next paragraphs that the approximation in ZK86 needs a slight correction.

The behaviour of the fractionation factors for two different trace species over a wide range of coupling parameters and primary species fluxes $i = H_2$, i.e. $\Phi_i = \Phi_{H_2}$ is shown in Fig. 4. Note that compared to the simulation shown in Fig. 3, also Table 1, we have moved the inner simulation radius to larger radii, and used open inner boundary conditions, which allows to relax the simulation to steady-state as now the flow time-scale throughout domain is lower. We compare solutions the different fractionation factors for He with $m_j = 4$ a.m.u. and an unnamed other species with $m_j = 10$ a.m.u.. In the left-hand panel in Fig. 4 the transition of the secondary species escaping flux at infinity from well-coupled to uncoupled becomes quite obvious. The secondary species radial profiles change accordingly – at high Φ_{H_2}, i.e. in the well-coupled regime, the velocity profile as well as the density scale height attained is that of the primary species, whereas in the uncoupled regime, the secondary species behaves independently. We emphasize that in the well-coupled regime the secondary escape flux is not identical to the primary escape flux, it merely scales with the density ratio at the lower simulation boundary $n_j/n_i(r_0)$.

We note further that in the uncoupled regime, equation (58) produces a slightly too high prediction for the secondary escape rate. The reason for this lies in the assumption by ZK86 that the secondary species remain subsonic, which increases its density at its sonic point.

We correct this by taking into account the note by ZK86 that in the correct limit, when both species experience supersonic escape, $u_j/u_i \to \sqrt{1/\mu}$ has to hold, because in this limit, the species' solutions are separate Parker winds. Therefore, we modify equation (58) by adding a factor $\sqrt{\mu}$ into the denominator, resulting in

$$x_j = \frac{\mu\Phi_i - (\mu - 1)}{\mu\Phi_i - \sqrt{\mu}(\mu - 1)\exp\left(-\omega_0(\mu\Phi_i - (\mu - 1))\right)}, \tag{64}$$

this is shown in Fig. 4 to be in much better agreement with our numerical findings. We take the good agreement between this modified formula and our numerical results as a sign of both being the correct, transonic solution. While analytically true, this uncoupled limit is physically suspicious, given that the two (or more) fluids are not collisionally coupled to each other, but retain their transonic outflows. Under such conditions the individual fluids would likely not remain collisional and the fluid approximation would break down, with the true escape rates being given by Jeans-like escape of particles (Volkov 2016).

6 RESULTS – RADIATION TRANSPORT

Our radiation transport scheme is a multiband, multispecies extension of the schemes presented in Commercon et al. (2011) and Bitsch et al. (2013); Lega et al. (2014), inspired by the formalism presented in Vaytet et al. (2012). The scheme is implicit and by construction conserves the sum of radiative and internal energies over any time-step. For those following applications, we also quietly move the upper band index S^b to a lower band index S_b for improved readability.

Before presenting numerical results, we introduce a generalization of the popular model for irradiated, plane-parallel planetary atmospheres by Guillot (2010). This model is based on the idea that the radiation can be split into the incoming stellar irradiation and the re-radiated bands, which is the approach taken in AIOLOS. Here, we have generalized the solution to include multiple bands for the stellar irradiation; the temperature as a function of optical depth is given by

$$T^4 = T_{\rm int}^4\left(\frac{3\tau}{4} + \frac{1}{4 f_{\rm H}}\right) + \sum_b \frac{3\mu_*}{4} f \frac{S_b^{\odot}}{\sigma_{\rm SB}}\left[\frac{1}{3 f_{\rm H}} + \frac{\mu_*}{\gamma_b} + \left(\frac{\gamma_b}{3\mu_*} - \frac{\mu_*}{\gamma_b}\right)\exp\left(-\tau\frac{\gamma_b}{\mu_*}\right)\right]. \tag{65}$$

Here, $T_{\rm int}$ is the internal luminosity of the planet expressed as a temperature, implemented via equation (39).

The irradiation temperature, a measure of a local radiation fields' energy content, is for the stellar irradiation $T_{{\rm irr},b}^4 = S_b/\sigma_{\rm SB}$, and the planetary equilibrium temperature for a zero albedo planet is related to $T_{\rm irr}$ via $T_{\rm eq}^4 = T_{\rm irr}^4/4$. The optical depth in the thermal radiation band is τ, and μ_* is the angle of incident radiation, assumed to be 1 in AIOLOS. The parameters $\gamma_b = \kappa_{\odot,b}/\kappa_{\rm R}$ are the ratio of the opacity to stellar irradiation in the different bands to the opacity to the outgoing thermal radiation, which is assumed to be constant over radius and time. The factor of f is included because AIOLOS is a 1D code and represents the redistribution geometry of stellar irradiation over the full planet (see Appendix A). The parameter $f_{\rm H}$ is a boundary condition that relates the radiation flux to the radiation intensity at the top of the atmosphere, i.e. $f_{\rm H} = H/J$ (where $F = 4\pi H$). Guillot

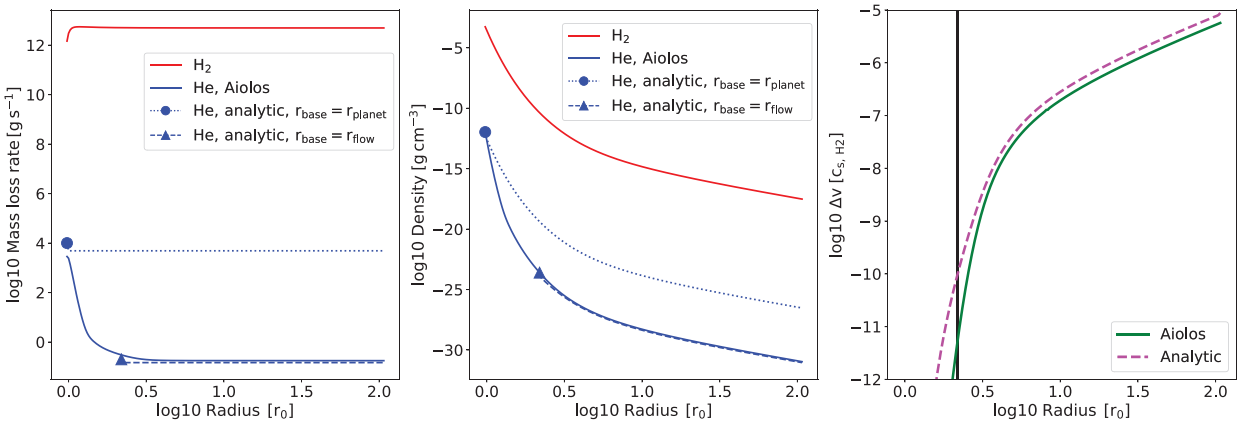

Figure 3. H_2/He coupled together via physical, i.e. non-constant collision constants, with He being a minor species. We compare mass-loss rates (**left**), density profiles (**middle**), and velocity differences (**right**) with the analytical solutions, based on two different choices of the lower radius r_0 in equation (58), as explained in the text. The blue dot denotes $r_{base} = r_{planet}$ and the resulting analytical profiles, and the blue triangle $r_{base} = r_{flow}$. The velocity differences between the two species (**right**) are discussed in the text. The black vertical line marks $r = r_{flow}$.

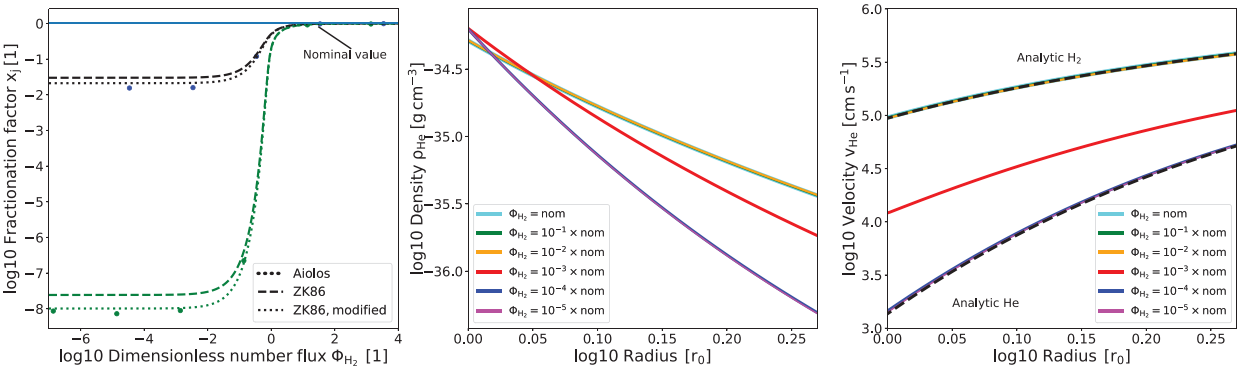

Figure 4. Varying the hydrogen density, i.e. the hydrogen escape flux for the same planet as in Fig. 3, but with $T = 8000$ K and a larger r_0, with the intention of showing the transition from well-coupled to decoupled two-species solutions for Helium (**Left**, black curves) and a $m_j = 10$a.m.u. species (**Left**, green curves). Density profile and the velocity profile of He (**Middle** and **Right**) adjust from high hydrogen flux to low hydrogen flux cases. It becomes evident that in the decoupled cases Helium converges on its own Parker-wind solution (**Right**).

Table 2. Important simulation parameters for all figures. The planet mass m_P, the lower simulation boundary radius r_0, the base density $\rho_0 \equiv \rho(r = r_0)$, the base temperature $T_0 \equiv T(r = r_0)$, and boundary types are listed. As unit, it is assumed that $r_{Jup} = 6.9911 \times 10^9$cm. For multiple species cases, initial base densities in Figs 3 and 4 are listed in the order of highest H_2 (subsequent runs decrease the H_2 abundance by 10^2 each), He, species 3 and for Figs 9 and 10 they are listed in the order of H_0, p^+, e^-. Additional parameters are listed in the text on a case-by-case basis. (∗) T_0 has been initialized with an adiabatic gradient, as opposed to isothermal for all other simulations. Boundaries are either walls/reflective (W) or open (O).

Figure	m_P ($m_\oplus$)	r_0 (cm)	$\approx r_0$ (r_{Jup})	ρ_0(g cm^{-3})	T_0 (K)	Lower boundary	Upper boundary
2, Dynamic	5	8×10^8	0.11	3×10^5	1.5×10^3	W	O
2, Static	224	9.4×10^9	1.34	8.28×10^{-8}	10^4	W	W
2, Dynamic	224	5×10^9	0.71	8×10^6	10^4	W	O
3	224	9.4×10^9	1.34	5×10^{-4}/ 1×10^{-12}	10^4	W	O
4	224	5.1×10^{10}	7.29	1.6×10^{-14}/ 7×10^{-35}/8×10^{-48}	8×10^3	O	O
5	224	9.15×10^9	1.31	1×10^{-5}	730	W	O
6,7,8	224	9.15×10^9	1.31	1×10^{-5}	730	W	O
9	21.25	2.75×10^9	0.39	2×10^{-12}/1×10^{-25}/5×10^{-29}	712	O	O
10	21.25	2.71×10^9	0.38	2.15×10^{-9}/1×10^{-25}/5×10^{-29}	712	W	O
11	33	2×10^{10}	2.8	2×10^{-5}	5×10^4∗	W	O

(2010) recommends $f_H = 1/2$ to match more detailed solutions for plane-parallel emission. However, the flux-limited diffusion (FLD, see equation 11) approximation traditionally assumes $H = J$ in the optically thin limit, which is appropriate for regions far from the emission surface where the geometry is no longer plane-parallel. We have included a factor ξ that corresponds to $1/f_H$ in AIOLOS' flux-limiter (see equation 12) and will thus compare our numerical solutions with both $\xi = 1$ and $\xi = 2$ to Guillot (2010)'s model.

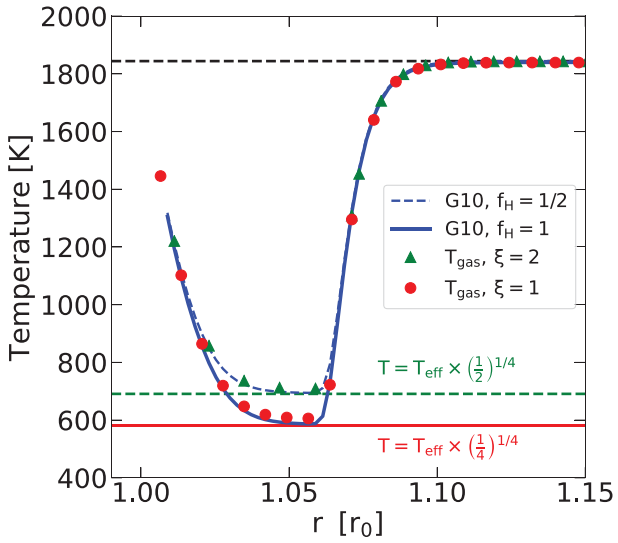

Figure 5. Middle-atmospheric temperature profiles after 10^{13} s in steady-state. We compare two solutions from (Guillot 2010) varying $f_H = H/K$ and equivalently, ξ in our simulations, with $\gamma = 10^2$. It is clear that $\xi = 2$ has to be used in order to get the correct minimum temperature in the atmosphere, which is $T_{\rm eff}/2^{1/4}$ when $\gamma \ll 1$ or $\gamma \gg 1$ (Dobbs-Dixon et al. 2012; Parmentier & Guillot 2014). The black dashed line marks the analytical value $S_1^{\odot}\gamma_1/(8\sigma_{\rm SB})^{1/4}$.

A property of equation (65) is that a characteristic temperature in the profile is $T_{\rm eff}^4 = \left(T_{\rm int}^4 + \frac{1}{4}T_{\rm irr}^4\right) = \left(T_{\rm int}^4 + T_{\rm eq}^4\right)$, when choosing their parameter values as $\mu_* = 1$(irradiation with zero angle w.r.t vertical), $f_H = 1/2$ (outer boundary condition), $f_K = 1/3$ (Eddington factor), and $f = 1/4$ (global average).

Finally, the minimum temperature appearing in a temperature profile, $T_{\rm min}^4$ lies between $T_{\rm eff}^4$ and $T_{\rm eff}^4/2$ (Parmentier & Guillot 2014) depending on the value of γ (the latter for $\gamma \to \infty$ or $\gamma \to 0$ and the former for $\gamma \to 2$). We discuss the conditions under which our numerical model can reproduce those low temperatures at intermediate altitudes in the next section, as this minimum temperature in the profile can form a cold trap (Catling & Kasting 2017, Chapt. 5) and thus severely limit the escape rates. The temperature in the upper atmosphere, in the limit $T(\tau \to 0)$ is termed the skin temperature and is $T_{\rm skin}^4 = \frac{1}{2}T_{\rm eff}^4 + \frac{\gamma}{4}T_{\rm eq}^4$.

It is a general feature of double-grey models that the temperature minimum is $T_{\rm min} \leq T_{\rm eff}$ in the temperature profile $T(r)$, which remains true in dedicated, line-by-line high-resolution studies of atmospheric temperature profiles (Parmentier et al. 2015, Fig. 18).

6.1 A comment on the FLD factor ξ

As noted previously, the factor ξ that appears in our flux limiter (equations 12 and 46) determines the FLD flux in the optically thin limit. The nominal value of $\xi = 1$ is widely used as standard in the literature and corresponds to a collimated beam of radiation, but it fails to reproduce the analytical solution for irradiated planetary atmospheres with the parameters $\mu_*, f_{\rm H}, f_{\rm K}, f$ as introduced before, see Fig. 5. To obtain a match between the FLD results and the analytical results we have to assume either $f_{\rm H} = 1$ in the Guillot (2010)-solution (corresponding to collimated radiation in the optically thin regions) or rescale our mean-free path parameter in the FLD solution via the choice $\xi = 2$. With $\xi = 2$ our hybrid FLD code obtains the correct temperature minimum, $T_{\rm eff} \times \left(\frac{1}{2}\right)^{1/4}$, of the semi-grey plane-parallel model and matches the analytical temperature profile Fig. 5. The re-scaling via $\xi = 2$ simply accounts for the fact that, in a plane-parallel geometry, the radiation field is not collimated. Instead there is a significant contribution from rays travelling laterally through the atmosphere that means the flux is only 1/2 of its free-streaming value (e.g. Dobbs-Dixon, Agol & Burrows 2012). This is the main reason for the introduction of the ξ-parameter in our code, and the user can choose between those values, depending on the application. The comparison is shown in Fig. 5. The instellation used in the only band was $S_1^{\odot} = 10^8\,{\rm erg\,cm^{-2}\,s^{-1}}$, $T_{\rm int} = 350$ K, and the opacity to the instellation $\kappa_1^{\odot} = 10^2\,{\rm cm^2\,g^{-1}}$, the Rosseland mean opacity was $\kappa_R = 1{\rm cm^2\,g^{-1}}$.

It is important to note that $\xi = 2$ may not always represent the best choice. The results of plane-parallel fully line-by-line radiative transfer models show that non-grey effects can cause the minimum temperature to be below that of the Guillot (2010)-type models (Parmentier et al. 2015). Although the non-grey effects could be accounted for by using a sufficient number of bands in the FLD calculation, one might find sufficient accuracy with fewer bands by tuning the choice of ξ. Another point of consideration is that the choice $\xi = 2$ is appropriate for a plane parallel geometry – far away from the planet the thermal radiation field must eventually become collimated, resulting in $\xi = 1$. The impact of this error will depend on γ: for large γ the skin temperature is not much affected by the thermal radiation emitted by the planet since $T_{\rm skin}^4 \approx \gamma T_{\rm eq}^4/4$, but for small γ the temperature far from the planet will be overestimated by a factor $\xi^{1/4}$ (1.189 for $\xi = 2$).

Finally, we note the residuals in Fig. 5 for the $\xi = 2$ model at $r = 1.06\,r_0$, i.e. the temperature minima, are T_{G10}–$T_{\rm min} \approx 6$ K and $T_{\rm AIOLOS}$–$T_{\rm min} \approx 25$ K. The larger differences between our code and the Guillot (2010) approximations are not surprising, given that we are not solving a plane-parallel but spherically symmetric geometry.

6.2 Single species, double-grey

After fixing $\xi = 2$, we show a number of important atmospheric prototypical temperature profiles in steady state ranging from $\gamma < 1$ to $\gamma > 1$, which correspond to greenhouse and antigreenhouse atmospheres. The steady-state is achieved by running a hydrostatic simulation (i.e. with the hydrodynamics module disabled) for a long time, after which radiative equilibrium is certainly established, in this case $>10^{13}$ s, i.e. $\sim$0.3 Myr. Irradiation and cooling radiation are focused in one band each, i.e. a setting corresponding to a double-grey model. Ingoing radiation is denoted $S_1(r)$, outgoing radiation $F_1(r)$. The planet in our simulation set to resemble HD 2094586b and its host star, i.e. a planet with $m_{\rm P} = 224\,m_{\oplus}$, $r_0 = 1.31 R_{\rm Jup}$, with the initial atmospheric density profile constructed from a isothermal solution at $T_{\rm init} = 730$ K, far from $T_{\rm eq} = 1340$ K (Cooper & Showman 2006), to show how the correct temperature is attained. Our choice of $R_{\rm P}$, while taken from the transit radius literature, here means only the radius of the inner simulation boundary, at which reflective boundaries are applied. The planet is orbiting a G0 star with $R = 1.2R_{\odot}$, $T_{\rm eff} = 6070$ K at a semimajor-axis distance of 0.05 au, emitting a perfect blackbody spectrum. The resulting stellar bolometric flux at the planet is $S_1^{\odot} = 9.66 \times 10^8\,{\rm erg\,cm^{-2}\,s^{-1}}$ and $T_{\rm int} = 350$ K. Opacities are identical to those used in the previous section. For reasons of simplicity, we set $\kappa_{\rm P} = \kappa_{\rm R}$.

The comparisons with equation (65) are shown in Figs 6 and 7. Skin temperatures and minimum temperatures as predicted by the preceding description are shown as lower and upper dashed lines. All temperature gradients are correctly reproduced by the numerical solution. In the middle and right-hand panel in Figs 6–8 we plot

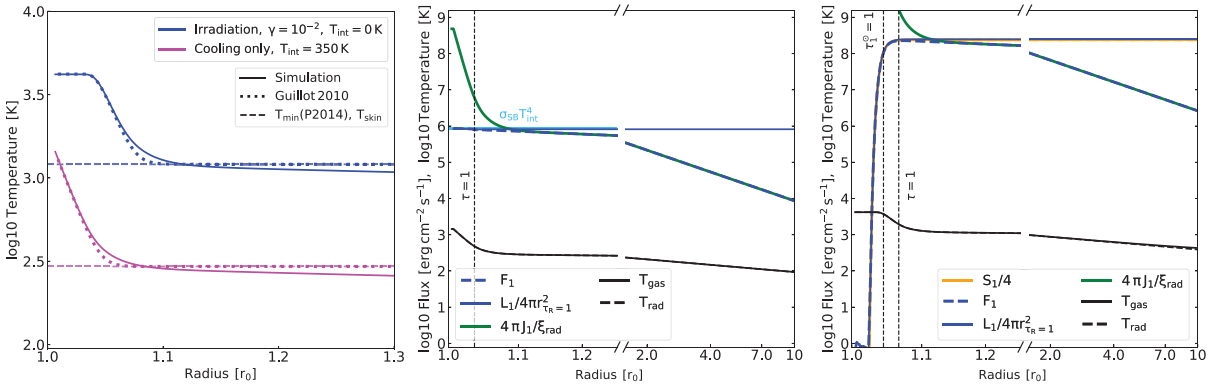

Figure 6. Comparisons for radiative quantities in steady-state. An atmosphere with only planetary luminosity (magenta curve, **left-hand** and **middle** panel) and $\gamma < 1$ irradiation without planetary luminosity (blue curve, **left-hand** and **right-hand** panel). The left-hand panel compares the temperature profiles with those from Guillot (2010) and shows the deviation from the Parmentier & Guillot (2014)-minimum temperature (dashed line, see text). Middle and right-hand panels show key radiative quantities for both simulations. Optically thin-thick transition radii to instellation and thermal reradiation are marked as dashed lines.

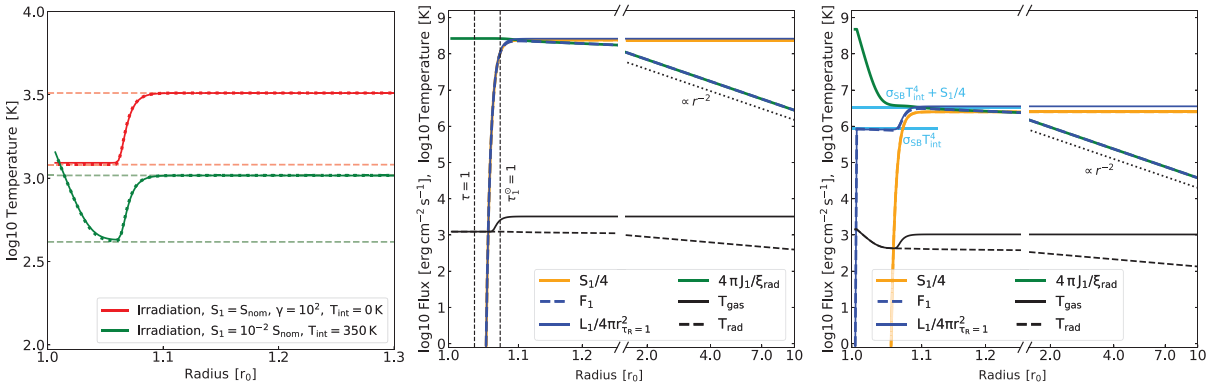

Figure 7. Same as Fig. 6, but for irradiation with $\gamma > 1$ without (red curve, **left-hand** and **middle** panel) and with planetary luminosity (green curve, **left-hand** and **right-hand** panel). A notable difference with Fig. 6 is $T_{\rm gas} > T_{\rm rad}$, due to the effects of inefficient re-radiation at $\gamma > 1$ in equation (65).

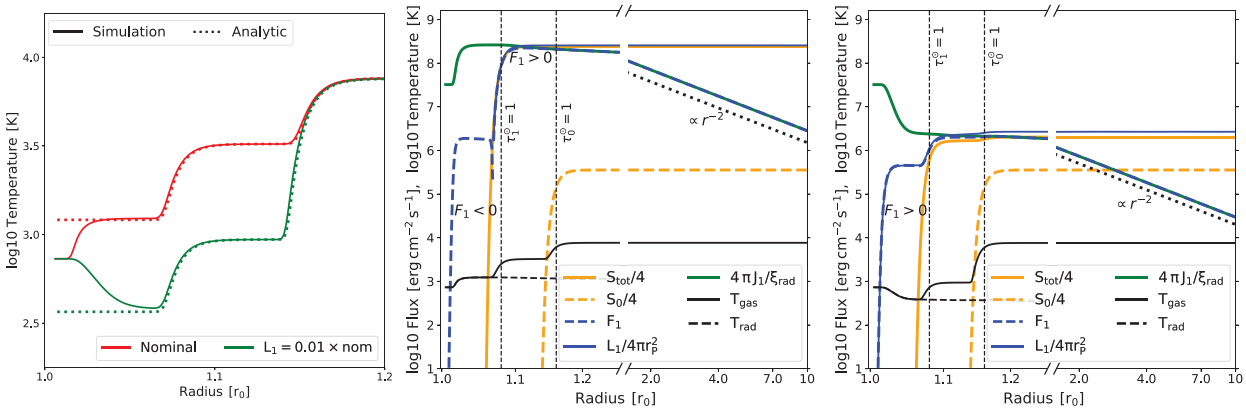

Figure 8. Same as Fig. 7, but for a two-band irradiation solution, which is not in steady-state, after $t = 10^6$ s. The nominal case (Red, **left** and **middle**) re-emits absorbed sunlight further downwards ($F_{\rm th} < 0$) and heats the atmosphere towards isothermality. The weakly irradiated case (Green, **left** and **right**) develops a cold stratosphere and the planet is instead adding its cooling luminosity to the total outgoing flux. Optically thick surfaces to the instellation in both bands are marked with $\tau_b^{\odot} = 1$, the Rosseland mean $\tau = 1$ radius is omitted.

important radiative quantities in order to check for code correctness and make it easier to understand the temperature profile.

First, we show a case without irradiation (magenta curve) in order to test the diffusive regime of the flux-limited radiation transport. The final numerical profile shows an identical slope in the deep parts of the atmosphere, and a slight upwards deviation from the analytical profile until the plane-parallel minimum temperature $T_{\rm min}$ is reached. From this point on, the temperature keeps decreasing, as $T_{\rm irr} = T_{\rm gas}$

is kept and flux density decreases via the $\nabla \cdot \boldsymbol{F}$-term in equation (9), which has a $\frac{1}{r^2}$-dependence in spherical coordinates instead of being constant as in a plane-parallel geometry.

The thermal re-radiation, i.e. re-radiation in band 1, $F_1 \equiv F_{\rm th}$ is shown as dashed blue line. The UV re-radiation F_0 is omitted, as it is completely negligible in both the numerical solution and the analytical solution. In the optically thin parts of the atmosphere it is evident that the free-streaming limit is correctly reproduced, i.e. $F_1 = 4\pi J_1/\xi$. The resulting planetary luminosity is $L = 4\pi r^2_{\tau=1} F_1$ and the flux is related to the internal temperature via $F_1(\tau = 1) = \sigma_{\rm SB} T^4_{\rm int}$. The $\tau = 1$-radius, $r_{\tau=1}$, is estimated numerically as the transition between the local Rosseland optically thick and thin cell transition and marked in the plots.

Next, we compare the profile of a irradiated, γ<1-atmosphere, which qualitatively shows similar behaviour to the internally heated case, with the same slope $\partial T/\partial\tau$. Also here the temperature decreases below the nominal minimum temperature. Note how in the cooling-only case the planet is clearly the source of the atmospheric luminosity, whereas for the irradiation-only case the planet merely re-radiates the incoming flux after heating towards the steady-state temperature. $T_{\rm irr}$ and $T_{\rm gas}$ remain at equilibrium, and the outgoing flux is 1/4 of the total stellar irradiation, or equivalently, $S_1/4 = L_1/(4\pi r^2_{\tau=1})$.

The case γ>1 with $T_{\rm int} = 0$ (see Fig. 7) is a typical case of a temperature inversion due to inefficient cooling, and shows radiative decoupling of $T_{\rm rad}$ and $T_{\rm gas}$. Finally, the case γ>1 with $T_{\rm int} = 350K$ shows inner and outer luminosity sources overlapping and raising the mid-altitude temperatures compared to the cooling-only case, although the absorption altitude is located much higher, at around $r = 1.05 r_0$.

The incoming stellar bolometric is plotted dashed orange curves. Those fluxes are absorbed at altitudes corresponding to their fixed values of γ_b. The thermal re-radiation, i.e. re-radiation in band 1, $F_1 \equiv F_{\rm th}$ is shown as dashed blue line. The UV re-radiation F_0 is omitted, as it is completely negligible in both the numerical solution and the analytical solution. In the optically thin parts of the atmosphere it is evident that the free-streaming limit is correctly reproduced, i.e. $F_1 = 4\pi J_1/\xi_{\rm rad}$ and $F \propto r^{-2}$. The resulting planetary luminosity is $L = 4\pi r^2 F_1$ and should agree in steady-state with the incoming stellar luminosity, when rescaled to the planetary surface, i.e. it should be $F_{\rm total} = L/(4\pi r_p^2)$. While the latter is close to being given in the case of the low-luminosity star, for the nominal case a larger deviation is evident. Here, a fraction of the luminosity is invested into heating the planet actively (the region marked with $F_1 < 0$, widening the gap between incoming radiation and planetary luminosity.

In the lower atmosphere, i.e. the stratosphere at $R < 1.05\, r_0$, where $\tau_1^{\odot} > 1$ but $\tau < 1$, the temperature is set by the condition $T = T_{\rm rad}$, where $T^4_{\rm rad} = J_1/(4\sigma_{\rm rad})$ is the radiation temperature of the total incoming stellar flux. In reality, this region would transition smoothly into a convective zone at the radiative-convective boundary, but convection is currently not implemented in the code.

6.3 Single species, non-equilibrium multiband with grey opacities

Here, we set-up a numerical test with two incoming radiation bands, S_0, S_1, two outgoing bands F_0, F_1 and one species evaluated against a Guillot (2010)-like analytical solution. In our numerical model, the two bands are bounded by $\lambda \in$ [0, 0.091],]0.091, ∞] μm. The outgoing radiation in F_0 corresponds to high-energy reradiation, which is always negligible in our models, hence for consistency reasons we also neglect it in the analytical treatment. By assigning a low flux, but high irradiation opacity for S_0, we can mimick the effects of a combined UV (S_0) and bolometric (S_1) irradiation scenario without the effects of ionization. We chose to show a non-equilibrium state after 10^6s simulation time in order to emphasize some important diagnostic features.

The previous planet and star parameters were kept, except that now the UV flux is $S_0^{\odot} = 10^6\,{\rm erg\,cm^{-2}\,s^{-1}}$ and $T_{\rm int} = 0$K. Without the photoionization module, the UV radiation simply acts as an additional bolometric heating source, depositing its full energy close to $\tau_0^{\odot} = 1$ for which the UV opacity $\kappa_0^{\odot} = 2 \times 10^6\,{\rm cm^2\,g^{-1}}$ was used.

The Planck-opacity ratios are set to constant values which now follow realistic estimates based on Malygin et al. (2014) and Lothringer et al. (2020) as $\gamma_0 = 2 \times 10^6$ and $\gamma_1 = 10^2$. This results in the absorption radii being located at $r_{\tau_0^{\odot}=1} \approx 1.160\, r_0$ and $r_{\tau_1^{\odot}=1} \approx 1.080\, r_0$. Two simulations are shown in Fig. 8, where the red curve is the run with all parameters as described, and the green curve has 100 times lower bolometric flux. For both cases the flux in the UV-band produces the same temperature, as according to equation (A), the deciding term is $\gamma_0 S_0 > \gamma_1 S_1$. The temperature in the region $1.05 < r/r_0 < 1.1$, in which it is $S_0 = 0$, is determined by $T^4 \propto \gamma_1 S_1$, i.e. is different in both simulations according to the difference in irradiation, same as $T_{\rm eff}/2^{1/4}$ in the lower atmosphere. A further difference is the temperature evolution in the deep, optically thick atmosphere. Here, the radiation diffusion time-scale can take a significant time, and compete with the hydrodynamic time-scales of outflows, i.e. it is important to check for convergence of outflow rates even after several sound-crossing times when radiative diffusion is considered. In those cases, a dependency on the initial conditions might be retained, which is mentioned in order to caution users of this code. In the cases presented we see both net heating and net cooling of the lowest part of the radiation from the reservoir of initial temperature at $r/r_0 < 1.3$, emphasized via $F_1 < 0$.

7 RESULTS – HIGH-ENERGY AND IONIZATION

We now turn to show a test of the ionization module. The data we compare to is taken from Owen & Alvarez (2016), and generated with an implementation of C^2-Ray (Mellema et al. 2006; Friedrich et al. 2012) in Zeus (Stone & Norman 1992). The planet has $m_{\rm P} = 21.25 m_{\oplus}$, a radius of $\rm r_0 = 0.394 \times r_{Jup}$, an atmospheric mass in the simulation domain of $2 \times 10^{-12}\, m_{\oplus}$ and an initial temperature of $T_{\rm eq} = 712\, K$, which we simultaneously use as lowest temperature floor, again identical to (Owen & Alvarez 2016).

Our UV irradiation is $\rm S_0^{\odot} = 4 \times 1.26 \times 10^6 erg\,cm^{-2}\,s^{-1}$ is compared with the ZEUS simulation having $\rm S_0^{\odot} = 1.26 \times 10^6 erg\,cm^{-2}\,s^{-1}$. This difference stems from our inclusion of the surface-averaging factor 1/4. Furthermore, a constant recombination coefficient of $\alpha = 2.7 \times 10^{-13}{\rm cm^{-3}}$ was used in both simulations which puts this outflow in the recombination-limited regime.

This comparison requires the thermal re-radiation in our code to be inefficient, for which we simply multiply the radiation–matter coupling terms $\kappa_P \rho (J - B)$ in equations (44) and (11) by a factor of 10^{-100}. This decouples the gas from the radiation field and hence only high-energy cooling terms come into effect, a situation identical to the physics in e.g. Sekiya et al. (1980), Watson et al. (1981), Tian & Toon (2005), Murray-Clay et al. (2009), and Salz et al. (2016). To reiterate, the equations solved are the ionization-equation, equation

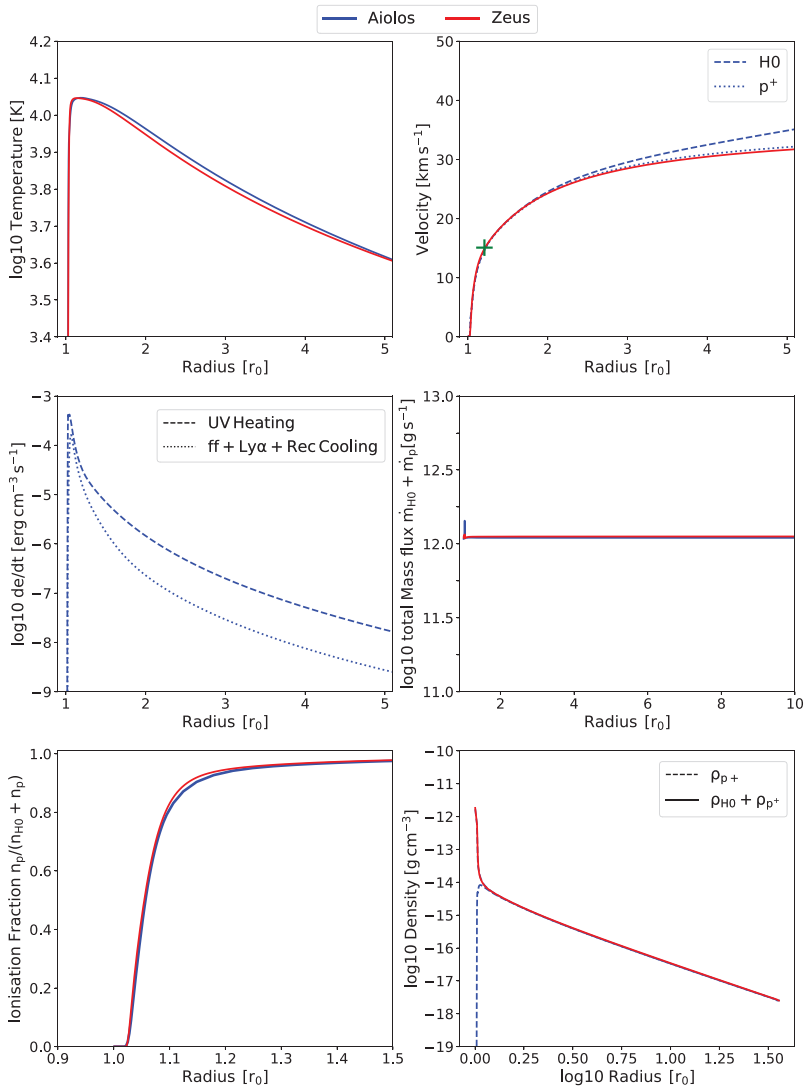

Figure 9. Results from the ionization module test for GJ 436b for the high UV irradiation case. Our simulation data shows the neutral hydrogen variables, unless otherwise specified, and is shown as blue dashed or blue dotted lines. The comparison simulation based on Owen & Alvarez (2016) but recomputed with ZEUS using the same recombination coefficient is shown in red (see text for details). The sonic point is noted as a green cross in the velocities (**Top Right**). Agreement between the two different numerical models is excellent, particularly in the total hydrogen escape rate, the key metric for escape models.

(47) along with the corresponding heating equations, equations (53)–(56). After the heating and cooling rates are computed and modified as a result of ionization, they are passed to the radiation solver, demonstrating its flexibility.

We then proceed to compare two limits identified as crucial in Murray-Clay et al. (2009), the advection-limited and recombination limited flows. Only the recombination-limited flow regime, i.e. the one occuring at high UV fluxes introduces new physics to our model, so we only plot this one. In both flux regimes our solutions show good agreement in the temperature, ionization rate, velocity and density variables, and excellent agreement down to better than 2 per cent in the escape mass flux for the total escape rate of $\dot{m}_H + \dot{m}_{p^+}$. This is shown in Fig. 9. It is interesting to note that the protons, representing the majority of mass in this region, have a velocity that follows the canonical simulation, whereas the neutral hydrogen is about to decouple from the flow and accelerates outward, as the flow becomes more ionized and momentum keeps getting added to the neutral hydrogen according to equation (49).

8 NEW APPLICATIONS

We show some new applications and proof-of-concept simulations which are possible with our code, which we intend to follow-up with stand-alone publications.

8.1 Thermally driven mass-loss and photoevaporation in the same simulation

Here, we aim to combine two different physical processes which are discussed in the literature. Core-powered mass-loss, which is an isothermal mass-loss process at $T = T_{\rm eq}$, could in principle be supported by UV-driven mass-loss (Bean, Raymond & Owen 2021) achieving typically $T \sim 10^4$ K in the upper atmosphere. However, so far no simulations unifying those physical processes and their drivers over the entire spectral range exist.

For this set of simulations, we simulate the atmospheric escape of atomic hydrogen from the previous model of GJ436b, however, now we include the bolometric radiation from the host M2-dwarf.

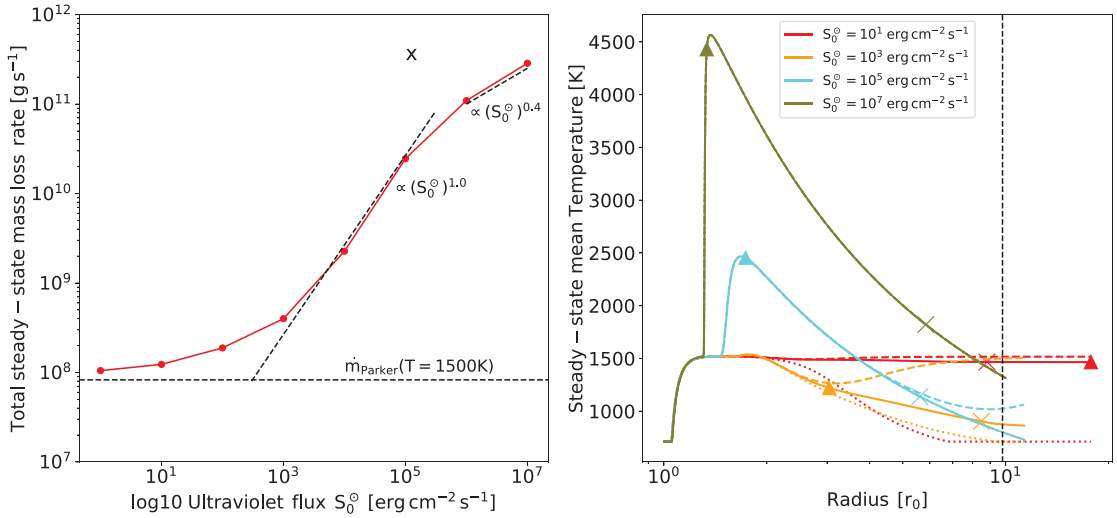

Figure 10. Combined bolometric and photoevaporative models for GJ 436b. The mass-loss rates (**Left**) show a transition from adiabatic nearly constant Parker-like core-powered mass-loss to energy-limited escape (seen as near-linear dependency on the UV flux) to recombination-limited mass-loss (seen as the high UV flux limit). The black cross marks a comparison simulation, for which the effects of bolometric heating and cooling have been switched off. The temperature profiles (**Right**) mark the sonic radius as crosses, the ionization front where $n_H = n_{p+}$ as triangle, and the Hill-radius as vertical dashed line. Dashed lines are the neutral hydrogen temperatures, dotted are protons, solid lines are the mass-weighted average of those temperatures. Electrons are thermalized with the protons for $S_0^{\odot} > 10^4 \mathrm{erg\,cm^{-2}\,s^{-1}}$, but thermally decoupled and hotter than the protons, for lower UV fluxes. This insufficient heating and adiabatic cooling results in cold outflowing protons.

We add a constant opacity to hydrogen in the bolometric band, in order to emulate absorption and efficient thermal heating by another species (which might be any molecular species, in a more complete simulation).

The setup consists of three species, (H, p^+, e^-), two incoming radiation bands with fluxes (S_0, S_1) again representing the UV and visible bands, $S_1^{\odot} = 1.1 \times 10^7\,\mathrm{erg\,cm^{-2}\,s^{-1}}$, resulting from $R_{star} = 0.415 R_{\odot}$, $T_{star} = 3370$K and a star–planet distance of $d = 0.05$au. We use one thermal band for the outgoing radiation F_{th}. Opacities for H are $(\kappa_0, \kappa_1, \kappa_{th}) = (1.1922 \times 10^6, 1, 10)\,\mathrm{cm^2\,g^{-1}}$. Thus, the visible radiation will be deposited in the lower atmosphere but result in lower temperatures compared to the UV radiation. The reason for this behaviour is identical to that given in Section 6.3. For $S_0^{\odot} = 0$ there will be only limited H escape, as lower atmospheric temperatures are then insufficient to push the entire atmospheric mass out of the gravitational well.

Atomic hydrogen starts in a hydrostatic state and the top-of-atmosphere radiation fluxes are ramped up in the first 10^3 s to their maximum values in both bands. We show the results in its hydrodynamic steady state after 4×10^6 s total simulation time, in Fig. 10.

It can be seen that at low UV fluxes the hydrogen escapes at a constant rate, close to the one given by the Parker wind. The simulation uses a tidal field with $M_{star} = 0.425 M_{\odot}$, whereas the analytical Parker wind does not, hence the escape rates are slightly higher. While the effect is only minor here, we think it should be worth investigating the importance of this increase in escape rate in the context of core powered mass-loss in future work around stars of different masses. Photoionization becomes relevant at higher $S_0^{\odot}$, the upper atmospheric hydrogen temperature rises and the adiabatic (energy-limited) escape regime takes over, finally reaching the recombination-limited escape regime at very high UV-fluxes. Those fluxes are not necessarily realistic for all stars, particularly GJ436, but merely serve to showcase the recombination-limit. We ran an additional simulation similar to what was shown in Fig. 9 in the energy-limited regime as reference case with $S_0^{\odot} = 1.25 \times 10^5\,\mathrm{erg\,cm^{-2}\,s^{-1}}$, but without the effects of bolometric heating and cooling, shown in Fig. 10 as black cross. In order to guarantee the same base density profile and location of the ionization front in the absence of bolometric heating, we used a lower floor temperature of $T_{floor} = 1500$ K for this simulation. As expected, without bolometric cooling the escape rate is drastically higher, by a factor of ∼14.1.

Because the solution for the temperature profile of irradiated planetary bodies presented by Guillot (2010) shows that the effects of stellar energy deposited deep in the atmosphere and an internal core-luminosity are indistinguishable, we understand the hydrogen escape rates found here at $S_0^{\odot}$ as analogous to core-powered mass-loss. However, an implementation of a core-luminosity and a systematic examination of the process presented here in the future are necessary for clarity of distinguishing between differing approaches.

As we increase the UV flux into the atmospheres and the escape rates move into an energy-limited mode, it is interesting to note that the temperature becomes a bad predictor of the overall escape rate. This is obvious in the simulation with $S_0^{\odot} = 10^3\,\mathrm{erg\,cm^{-2}\,s^{-1}}$, which shows in Fig. 10 a cold trap in the temperature profile in both the neutral and ionized hydrogen, but higher total escape rates compared to lower UV fluxes. We understand this to be a result of the flow time-scale of the Parker solution (Cranmer 2004) being shorter at that particular UV absorption radius than the cooling time-scale given by the Planck opacity.

Finally, the tidal field we used is to be seen as a numerical aid in reaching a steady state solution. While the heated lower atmosphere is expanding into the upper atmosphere in the initial phases of the simulation($t < 10^3$ s), shocks occur, which slow the runs dramatically. The tidal field helps to remove the upper atmosphere quickly before shocks can form. However generally, care needs to be taken, as tidal fields are also known to have an influence on the final steady-state of the outflow (Erkaev et al. 2007; Murray-Clay et al. 2009).

8.2 Fully time-dependent, radiative simulation of gas giant formation

We now demonstrate the capability of the code to form a giant planet in a radiative core-accretion simulation. Traditional approaches (Pollack et al. 1996; Mordasini et al. 2012) use a stepping between steady-states in order to solve this problem, whereas we are capable of following the planets' formation in a fully time-dependent manner. In the core-accretion scenario, giant planets first accrete an envelope less massive than its core. This envelope slowly cools and contracts over a significant time, dubbed the hydrostatic phase. Once the first mass-doubling is reached, the contraction accelerates due to the action of the self-gravity of the gas. The accelerated contraction forces the gas to cool more intensely, which increases the accretion rate, again increasing the contraction rate. This process is called runaway gas-accretion. The runaway phase self-terminates in the classical literate once a disc-limited accretion rate is reached. In our case, however, we do not impose a limit on the accretion rate. Instead, we imposed open boundary conditions which results in runaway accretion only slowing down when the simulation domain fills up with gas.

For the sake of simplicity, and to accelerate the formation of the gas giant, we follow the approach of Ayliffe & Bate (2012) and use a seed core mass of 33 $m_\oplus$, a domain size of $[r_0, r_{\max}] = [2.8,\ 1.2 \times 10^4]\, r_{\rm Jup}$ and a constant opacity in the entire simulation domain of $\kappa = 10^{-2}\,{\rm cm^2\,g^{-1}}$. Note that this r_0 at the given mass would yield a core of unphysically low density. We do not include the effects of convection, or hydrogen dissociation in this example calculation. We use a simulation domain size of the spatial resolution was 50 simulation cells per decade, resulting in a total of 185 cells. As our simulations are 1D, the computation of self-gravity is achieved via the usage of the shell theorem, with the integrated mass $M(r) = 4\pi \int_0^r {\rm d}r' r'^2 \rho(r')$ being used to re-compute the gravitational potential $\Phi(r) = GM(r)/r$ at every time-step.

The initial density profile is constructed using an adiabatic temperature structure, starting from a disc density at the simulation boundary of $\rho_0 = 3 \times 10^{-13}\,{\rm g\,cm^{-3}}$ at an initial entropy $\ln(p/\rho^\gamma) = 30.27$ with $\gamma = 1.4$. This puts most the initial mass at large radii, but the planetary structure compactifies with time as it cools. Already after 10 yr is the initial mass centrally concentrated. Our giant planet forms within 1500 yr, as can be seen in Fig. 11, reaching $\sim 8 M_{\rm Jup}$, at which point we terminate the simulation, while it reaches crossover mass after ~ 600 yrs. Those short time-scales are found due to our very high choice of initial core mass, and the very low opacity. A first peak in the luminosity curve, at ~ 100 yrs is due to the initial accretion of an envelope, until a hydrostatic solution is found that fills the planetary gravitational potential at given entropy. After the planet reaches a mass of $\sim 2 M_{\rm Jup}$ at 900 yr, the simulation domain is filled up with quasi-hydrostatic gas again, as in the initial condition. The mass distribution then changes shape towards more mass being located at large radii again. However, a high luminosity from ongoing contraction allows the planet to continue accreting. At this point the Hill-radius of the planet would be larger than the disc-scale height ($r_H \sim 0.2$ au compared to $H_{\rm disc} \sim 0.156$ au for a disc with $h/r = 0.03$, a lower limit for irradiated discs (Bitsch et al. 2013), and 3D effects would need to be taken into account (Kley, D'Angelo & Henning 2001; Tanigawa et al. 2012; Szulágyi et al. 2016; Schulik et al. 2020). The simulation is stopped after an arbitrary time, 1500 yr in this case. Final planet masses are presumably set by gap-opening (Ayliffe & Bate 2009). Furthermore, it is known that the slow phase of quasi-hydrostatic growth can be lengthened by recycling the outer envelope entropy into the protoplanetary disc (Cimerman, Kuiper & Ormel 2017), as well shortened by effects of dust growth (Movshovitz et al. 2010) and accreted dust has non-constant properties (Öberg, Murray-Clay & Bergin 2011; Booth et al. 2017), effects which to model is beyond the scope of this work.

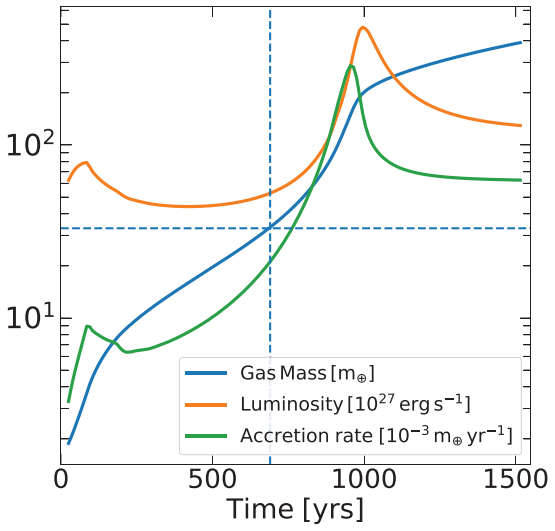

Figure 11. Fully time-dependent giant planet model, including runaway gas accretion, starting with a core mass of 33$m_\oplus$ and constant gas opacity of $\kappa = 10^{-2}\,{\rm cm^2\,g^{-1}}$. The crossover-point in mass is marked with a horizontal and vertical dashed line, at around 700 yrs, at which point gravitational self-contraction of the envelope becomes important, and the increase in luminosity starts supporting higher contraction rates, resulting in runaway gas-accretion and the formation of a $8.2 M_{\rm Jup}$ gas giant.

9 FUTURE WORK AND SUMMARY

We have presented a new multispecies, multiphysics hydrodynamic code, AIOLOS, designed for simulating accretion onto, and hydrodynamic escape from, planetary atmospheres. We present a wide range of tests for the code. These include standard hydrodynamic and radiation hydrodynamic tests, along with a suite of problem-specific tests. We benchmark our code's results against existing models of atmospheric escape, such as EUV-driven mass-loss from hot Jupiters and the entrainment of trace species in an evaporative wind. For the first time, we demonstrate agreement between the atmospheric temperature structure computed by radiation transport computed in flux-limited diffusion approximation and analytical atmosphere models (Guillot 2010). Finally, we present new proof-of-concept calculations showing the transition between EUV-driven and thermally driven mass-loss (also known as core powered mass-loss, e.g. Gupta & Schlichting 2019). We also demonstrate the transition between between cooling-dominated and runaway gas accretion onto giant planets in a fully dynamical simulation.

AIOLOS is already being applied to a range of problems. Booth et al. (2023) used AIOLOS to model dust formation in the winds of ultrashort period planets.

Already in e.g. Cooper & Showman (2006), it was shown that non-equilibrium chemistry in the atmospheres of hot Jupiters can be very important, when the advective time-scale is shorter than the kinetic time-scale. For this reason, coupling with deep atmospheric codes, as well as a more advanced chemical solver seems like a necessary step to implement in the near-future.

In upcoming work, we will furthermore explore the physics of full-spectrum atmospheric escape models with realistic opacities, which

should prove to be a dramatic improvement over the simplistic results shown in Fig. 10. Furthermore, the ionization of multiple species, such as He, C, and O, and the transition from a molecular to atom-dominated atmosphere need to be addressed with an extension of the photochemistry scheme shown in this work. This work, once fulfilled, should provide valuable insight into the evolution and current state of the exoplanetary population.

ACKNOWLEDGEMENTS

The authors thank the anonymous referee for significantly improving the manuscript. We thank James Owen for discussions and providing the ZEUS simulation data. MS would like to thank Shun Fai Ling for proofreading. RAB is supported by the Royal Society through University Research Fellowships. This project has received funding from the European Research Council (ERC) under the European Union's Horizon 2020 research and innovation programme (Grant agreement No. 853022, PEVAP). For the purpose of open access, the authors have applied a Creative Commons Attribution (CC-BY) licence to any Author Accepted Manuscript version arising. This project has recieved support from a 2020 Royal Society Enhancment Award.

DATA AVAILABILITY

For the purpose of open access, the authors have applied a Creative Commons Attribution (CC-BY) licence to any Author Accepted Manuscript version arising. The EIGEN library is an open source package and available under eigen.tuxfamily.org. AIOLOS is an open source code and is available on github.

REFERENCES

Ayliffe B. A., Bate M. R., 2009, MNRAS, 393, 49
Ayliffe B. A., Bate M. R., 2012, MNRAS, 427, 2597
Baraffe I., Selsis F., Chabrier G., Barman T. S., Allard F., Hauschildt P. H., Lammer H., 2004, A&A, 419, L13
Bean J. L., Raymond S. N., Owen J. E., 2021, J. Geophys. Res., 126, e06639
Benítez-Llambay P., Krapp L., Pessah M. E., 2019, ApJS, 241, 25
Bitsch B., Crida A., Morbidelli A., Kley W., Dobbs-Dixon I., 2013, A&A, 549, A124
Bodenheimer P., Pollack J. B., 1986, Icarus, 67, 391
Bondi H., 1952, MNRAS, 112, 195
Booth R. A., Clarke C. J., Madhusudhan N., Ilee J. D., 2017, MNRAS, 469, 3994
Booth R. A., Owen J. E., Schulik M., 2023, MNRAS, 518, 1761
Caldiroli A., Haardt F., Gallo E., Spinelli R., Malsky I., Rauscher E., 2021, A&A, 655, A30
Catling D. C., Kasting J. F., 2017, Atmospheric Evolution on Inhabited and Lifeless Worlds. Cambridge University Press, Cambridge
Cimerman N. P., Kuiper R., Ormel C. W., 2017, MNRAS, 471, 4662
Colella P., Woodward P. R., 1984, J. Comput. Phys., 54, 174
Commercon B., Teyssier R., Audit E., Hennebelle P., Chabrier G., 2011, A&A, 529, A35
Cooper C. S., Showman A. P., 2006, ApJ, 649, 1048
Cranmer S. R., 2004, Am. J. Phys., 72, 1397
D'Angelo G., Kley W., Henning T., 2003, ApJ, 586, 540
Dobbs-Dixon I., Agol E., Burrows A., 2012, ApJ, 751, 87
Erkaev N. V., Kulikov Y. N., Lammer H., Selsis F., Langmayr D., Jaritz G. F., Biernat H. K., 2007, A&A, 472, 329
Erkaev N. V. et al., 2013, Astrobiology, 13, 1011
Font A. S., McCarthy I. G., Johnstone D., Ballantyne D. R., 2004, ApJ, 607, 890
Freedman R. S., Lustig-Yaeger J., Fortney J. J., Lupu R. E., Marley M. S., Lodders K., 2014, ApJS, 214, 25
Friedrich M. M., Mellema G., Iliev I. T., Shapiro P. R., 2012, MNRAS, 421, 2232
Fulton B. J. et al., 2017, AJ, 154, 109
García Muñoz A., 2007, Planet. Space Sci., 55, 1426
Ginzburg S., Schlichting H. E., Sari R., 2018, MNRAS, 476, 759
Gottlieb S., Shu C.-W., Tadmor E., 2001, SIAM Rev., 43, 89
Greenberg J. M., Leroux A. Y., 1996, SIAM J. Num. Anal., 33, 1
Guillot T., 2010, A&A, 520, A27
Gunell H., Maggiolo R., Nilsson H., Stenberg Wieser G., Slapak R., Lindkvist J., Hamrin M., De Keyser J., 2018, A&A, 614, L3
Gupta A., Schlichting H. E., 2019, MNRAS, 487, 24
Gupta A., Schlichting H. E., 2020, MNRAS, 493, 792
Ho C. S. K., Van Eylen V., 2023, MNRAS, 519, 4056
Hubeny I., 1990, ApJ, 351, 632
Hui L., Gnedin N. Y., 1997, MNRAS, 292, 27
Hunten D. M., 1973, J. Atmos. Sci., 30, 1481
Johnstone C. P., Güdel M., Lammer H., Kislyakova K. G., 2018, A&A, 617, A107
Käppeli R., Mishra S., 2014, J. Comput. Phys., 259, 199
Käppeli R., Mishra S., 2016, A&A, 587, A94
Kley W., 1989, A&A, 208, 98
Kley W., 1998, A&A, 338, L37
Kley W., D'Angelo G., Henning T., 2001, ApJ, 547, 457
Kubyshkina D. et al., 2018, ApJ, 866, L18
Kubyshkina D. et al., 2019, ApJ, 879, 26
Kuiper R., Klahr H., Dullemond C., Kley W., Henning T., 2010, A&A, 511, A81
Lammer H., Selsis F., Ribas I., Guinan E. F., Bauer S. J., Weiss W. W., 2003, ApJ, 598, L121
Lammer H., Kasting J. F., Chassefière E., Johnson R. E., Kulikov Y. N., Tian F., 2008, Space Sci. Rev., 139, 399
Lee E. J., Connors N. J., 2021, ApJ, 908, 32
Lee E. J., Karalis A., Thorngren D. P., 2022, ApJ, 941, 186
Lega E., Crida A., Bitsch B., Morbidelli A., 2014, MNRAS, 440, 683
Levermore C. D., Pomraning G. C., 1981, ApJ, 248, 321
Lothringer J. D., Fu G., Sing D. K., Barman T. S., 2020, ApJ, 898, L14
Malygin M. G., Kuiper R., Klahr H., Dullemond C. P., Henning T., 2014, A&A, 568, A91
Mayor M. et al., 2011, preprint(arXiv:1109.2497)
McCann J., Murray-Clay R. A., Kratter K., Krumholz M. R., 2019, ApJ, 873, 89
Mellema G., Iliev I. T., Alvarez M. A., Shapiro P. R., 2006, New Astron., 11, 374
Mignone A., 2014, J. Computat. Phys., 270, 784
Mizuno H., Nakazawa K., Hayashi C., 1978, Prog. Theor. Phys., 60, 699
Mordasini C., Alibert Y., Klahr H., Henning T., 2012, A&A, 547, A111
Movshovitz N., Bodenheimer P., Podolak M., Lissauer J. J., 2010, Icarus, 209, 616
Murray-Clay R. A., Chiang E. I., Murray N., 2009, ApJ, 693, 23
Öberg K. I., Murray-Clay R., Bergin E. A., 2011, ApJ, 743, L16
Öpik E. J., 1963, Geophys. J., 7, 490
Owen J. E., 2019, Ann. Rev. Earth Planet. Sci., 47, 67
Owen J. E., Alvarez M. A., 2016, ApJ, 816, 34
Owen J. E., Jackson A. P., 2012, MNRAS, 425, 2931
Owen J. E., Wu Y., 2017, ApJ, 847, 29
Parker E. N., 1958, ApJ, 128, 664
Parker E. N., 1965, Space Sci. Rev., 4, 666
Parmentier V., Guillot T., 2014, A&A, 562, A133
Parmentier V., Guillot T., Fortney J. J., Marley M. S., 2015, A&A, 574, A35
Piso A.-M. A., Youdin A. N., 2014, ApJ, 786, 21
Pollack J. B., Hubickyj O., Bodenheimer P., Lissauer J. J., Podolak M., Greenzweig Y., 1996, icarus, 124, 62
Press W. H., Teukolsky S. A., Vetterling W. T., Flannery B. P., 2002, Numerical Recipes in C++ : The Art of Scientific Computing. Cambridge University Press, Cambridge
Rogers J. G., Owen J. E., 2020, MNRAS, 503, 1526
Rogers J. G., Gupta A., Owen J. E., Schlichting H. E., 2021, MNRAS, 508, 5886

Salz M., Banerjee R., Mignone A., Schneider P. C., Czesla S., Schmitt J. H. M. M., 2015, A&A, 576, A21
Salz M., Schneider P. C., Czesla S., Schmitt J. H. M. M., 2016, A&A, 585, L2
Schulik M., Johansen A., Bitsch B., Lega E., Lambrechts M., 2020, A&A, 642, A187
Schunk R. W., 1977, Rev. Geophys. Space Phys., 15, 429
Schunk R. W., Nagy A. F., 1980, Rev. Geophys. Space Phys., 18, 813
Sekiya M., Nakazawa K., Hayashi C., 1980, Prog. Theor. Phys., 64, 1968
Stone J. M., 1997, ApJ, 487, 271
Stone J. M., Norman M. L., 1992, ApJS, 80, 753
Stone J. M., Gardiner T. A., Teuben P., Hawley J. F., Simon J. B., 2008, ApJS, 178, 137
Szulágyi J., Masset F., Lega E., Crida A., Morbidelli A., Guillot T., 2016, MNRAS, 460, 2853
Tanigawa T., Ohtsuki K., Machida M. N., 2012, ApJ, 747, 47
Tian F., Toon O. B., 2005, Geophys. Res. Lett., 32, L18201
Toro E., 2009, Riemann Solvers and Numerical Methods for Fluid Dynamics: A Practical Introduction. Springer Berlin, Heidelberg
Toro E. F., Spruce M., Speares W., 1994, Shock Waves, 4, 25
Toth G., 1995, MNRAS, 274, 1002
Van Eylen V., Agentoft C., Lundkvist M. S., Kjeldsen H., Owen J. E., Fulton B. J., Petigura E., Snellen I., 2018, MNRAS, 479, 4786
Vaytet N., Audit E., Chabrier G., Commerçon B., Masson J., 2012, A&A, 543, A60
Vaytet N., González M., Audit E., Chabrier G., 2013, J. Quantum Spectrosc. Radiat. Transfer, 125, 105
Vidal-Madjar A. et al., 2004, ApJ, 604, L69
Volkov A. N., 2016, MNRAS, 459, 2030
Watson A. J., Donahue T. M., Walker J. C. G., 1981, Icarus, 48, 150
Wuchterl G., 1990, A&A, 238, 83
Yelle R. V., 2004, Icarus, 170, 167
Zahnle K. J., Kasting J. F., 1986, Icarus, 68, 462
Zeng L. et al., 2019, Proc. Natl Acad. Sci., 116, 9723

APPENDIX A: DERIVATION OF MULTIBAND GUILLOT-TYPE SOLUTIONS

Here, we provide a brief derivation of equation (65), a multiband generalization of Guillot (2010)'s approximate solution to the radiative transfer problem in plane-parallel atmospheres. Similar extensions already exist (e.g. Parmentier & Guillot 2014); however, we include our derivation since we retain some additional free parameters, such as $f_{\rm H}$ (defined below). We begin from the time-independent radiative-transfer equation for J (equation 9), and consider only one band for the re-emitted radiation, but multiple bands for the stellar heating. By neglecting the hydrodynamic terms and assuming thermal equilibrium we may work with a single species without loss of generality. Together, these provide the starting point:

$$\frac{{\rm d}H}{{\rm d}x} = -\rho\kappa_{\rm P}\left[J - \frac{\sigma_{\rm SB}T^4}{\pi}\right] \tag{A1}$$

$$H = -\frac{1}{3\rho\kappa_{\rm R}}\frac{{\rm d}J}{{\rm d}x} \tag{A2}$$

$$0 = \rho\kappa_{\rm P}\left[J - \frac{\sigma_{\rm SB}T^4}{\pi}\right] + f\sum_b \frac{S_{\odot,b}}{4\pi}\exp(-\tau_{\odot,b}/\mu)\rho\kappa_{\odot,b}. \tag{A3}$$

Here, we have explicitly kept the distinction between the Planck- and Rosseland-mean opacities in thermal bands. We have introduced $H = F/4\pi$ for ease of comparison with Guillot (2010) and also assumed the Eddington closure ($f_{\rm K} = 1/3$ in the notation of Guillot 2010), denoted by μ the angle of the incident radiation, and introduced a factor f that denotes how the stellar radiation is averaged over the planet. This factor should not be confused with f^b as used earlier in our numerical formulation, as in e.g. equation (43), where it denotes the fraction of the Planck integral in band b. $f = 1/4$ would be the usual isotropic average, which is used in AIOLOS, while $f = 1$ would be the valid at the sub-stellar point ($\mu = 1$).

Under the assumption that the various different opacities are constant, equations (A1) and (A3) may be solved together to give:

$$H(\tau) = H(0) + f\sum_b \frac{S_{\odot,b}}{4\pi}\left[1 - \exp(-\tau\gamma_b/\mu)\right]\gamma_{\rm P}\mu, \tag{A4}$$

where we now explicitly denote τ as the Rosseland optical depth to thermal radiation, $\tau = \int \rho\kappa_{\rm R}{\rm d}x$ and introduced the factors $\gamma_b = \kappa_{\odot,b}/\kappa_{\rm R}$ and $\gamma_{\rm P} = \kappa_{\rm P}/\kappa_{\rm R}$. This choice of optical depth scale is arbitrary but follows Parmentier & Guillot (2014) and has the effect that $\tau_{\odot,b} = \gamma_b\tau$. Following Guillot (2010), we associate the flux at large optical depth with the planet's internal luminosity, $H(\infty) = \sigma_{\rm SB}T_{\rm int}^4/4\pi$. Hence, $H(0) = \sigma_{\rm SB}T_{\rm int}^4/4\pi - f\sum_b \frac{S_{\odot,b}}{4\pi}\gamma_{\rm P}\mu$.

We can now integrate equation (A2), obtaining

$$J(\tau) = J(0) + 3H(\infty)\tau + 3f\sum_b \frac{S_{\odot,b}}{4\pi}\frac{\mu^2}{\gamma_b}\left[1 - \exp(-\tau\gamma_b/\mu)\right], \tag{A5}$$

where $\gamma_R = \kappa_R/\kappa_{\rm P}$. To close these equations we need an expression for $J(0)$. As in Guillot (2010), we express $J(0)$ in terms of the Eddington factor $f_{\rm H} = H(0)/J(0)$. Together with equation (A3), this gives:

$$T^4 = T_{\rm int}^4\left[\frac{3}{4}\tau + \frac{1}{4f_{\rm H}}\right] + \sum_b \frac{3\mu}{4}f\frac{S_{\odot,b}}{\sigma_{\rm SB}}\left[\frac{1}{3f_{\rm H}} + \frac{\mu}{\gamma_b} + \left(\frac{1}{3\mu}\frac{\gamma_b}{\gamma_P} - \frac{\mu}{\gamma_b}\right)\exp(-\tau\gamma_b/\mu)\right]. \tag{A6}$$

In the main text we consider only $\kappa_{\rm R} = \kappa_{\rm P}$, i.e. $\gamma_{\rm P} = 1$, and $\mu = 1$. Finally, it is worth considering the appropriate choice of the Eddington factor, $f_{\rm H}$. Guillot (2010) recommends $f_{\rm H} = 1/2$ since it agrees with more detailed solutions that take into account the anglular-dependence of the radiative-transfer equation. AIOLOS, however, uses the flux-limited diffusion approximation (FLD) to solve the radiative-transfer problem. In FLD, the flux in optically thin regions is limited by causality, i.e. radiation must not travel faster than the speed of light. This implies that $J = H$ in such regions and therefore we should expect $f_{\rm H} = 1$ to give better agreement with the numerical solutions computed with AIOLOS. $f_{\rm H}$ is only important around $\tau \sim 1$, however, so the differences can be expected to be limited to a small region.

This paper has been typeset from a TEX/LATEX file prepared by the author.